

# Materials Advances

Accepted Manuscript

This article can be cited before page numbers have been issued, to do this please use: R. Hossain, S. Khanom, P. Mondal and F. Ahmed, *Mater. Adv.*, 2025, DOI: 10.1039/D5MA00169B.



This is an Accepted Manuscript, which has been through the Royal Society of Chemistry peer review process and has been accepted for publication.

Accepted Manuscripts are published online shortly after acceptance, before technical editing, formatting and proof reading. Using this free service, authors can make their results available to the community, in citable form, before we publish the edited article. We will replace this Accepted Manuscript with the edited and formatted Advance Article as soon as it is available.

You can find more information about Accepted Manuscripts in the [Information for Authors](#).

Please note that technical editing may introduce minor changes to the text and/or graphics, which may alter content. The journal's standard [Terms & Conditions](#) and the [Ethical guidelines](#) still apply. In no event shall the Royal Society of Chemistry be held responsible for any errors or omissions in this Accepted Manuscript or any consequences arising from the use of any information it contains.

# Signature of half-metallicity and pressure-induced physical properties of Cubic $\text{ACrO}_3$ ( $A = \text{Si, Ge, Sn}$ ) multiferroic by DFT calculation

Rony Hossain<sup>a</sup>, Mst. Shamima Khanom<sup>a</sup>, Prianka Mondal<sup>b</sup>, Farid Ahmed<sup>a</sup>

<sup>a</sup>Department of Physics, Jahangirnagar University, Savar, Dhaka, 1342, Bangladesh

<sup>b</sup>Dhaka University of Engineering & Technology, Gazipur, 1707, Bangladesh

## Abstract

We report a comprehensive first-principle investigation of the structural, electronics, elastic, magnetic, and optoelectronics, and half metallicity of  $\text{ACrO}_3$  ( $A = \text{Si, Ge, Sn}$ ) with space group (Pm3m) (no.221) studied for the first time based on Density Functional Theory (DFT) under pressure 0-30GPa. The tolerance factor reveals the compound cubic phase. The robust characteristics of the compound  $\text{SnCrO}_3$  found at 3.78 Å robust transition lattice constant. The optimized stable magnetic state of the compound is ferromagnetic, and by applying Born stability criteria for elastic constants, it is found that  $\text{ACrO}_3$  ( $A = \text{Si, Ge, Sn}$ ) is mechanically stable in the whole pressure range. The material's half-metallic nature is confirmed by band gaps and density of states (DOS) studies, which show that the majority spin-channel states are conducting and the minority spin-down levels are semiconducting. Moreover, bulk(B) and shear modulus(G), Poisson's ratio( $\nu$ ), Cauchy pressures, Anisotropic factor(A), Plasticity measurement( $B/C_{44}$ ) and Young's modulus(E), we found plasticity and bond distortion decreases as pressure rises and materials  $\text{SnCrO}_3$  and  $\text{SiCrO}_3$  exhibit brittleness at 0 and 10-GPa and ductile at other pressure range. On the other hand,  $\text{GeCrO}_3$  exhibits a ductile nature in the whole pressure range. The spin-polarized band structure reveals that  $\text{ACrO}_3$  ( $A = \text{Si, Ge, Sn}$ ) maintains a direct band (R-R) gap at the whole pressure range. Several optical properties, including dielectric function, reflectivity, refractive index, conductivity, and absorption coefficient, are also calculated. It is revealed from the real part of the dielectric function that the compound is optically metallic at low energy regions, where it exhibits a semiconducting nature at higher energy regions and plasma frequency rises with pressure. The optical properties and half-metallic response show that  $\text{ACrO}_3$  ( $A = \text{Si, Ge, Sn}$ ) has intriguing properties for spintronic and optoelectronic devices.

**Keywords:** DFT; Multiferroic materials; Half-metallicity; High-pressure,  $\text{ACrO}_3$  ( $A = \text{Si, Ge, Sn}$ ); Curie temperature; Electronic structure; Elastic; Optical; Magnetic properties.



## 1. Introduction

These days, every electronic gadget operates on the principle of electron control, which creates a binary system by considering whether or not electrons are flowing through a circuit. However, because of their limited computing power, the computer industry thinks that we have reached the edge of this kind of device [1,2]. . As a result, researchers everywhere are concentrating on substitutes for electrical gadgets, with spintronics emerging as a promising choice. In other words, spintronic devices can improve device power by up to ten thousand times thanks to their octane coding based on the electron's spin [3,4]. Emerging technologies require developing new materials that meet particular requirements. Specifically, magnetic materials with stable structures, good electrical properties, and potential for thin-film application are needed for spintronic devices [5,6]. The vast majority of materials used in electronic devices are semiconductors. Since a magnetic behavior may be generated through the doping procedure with magnetic species, such materials can be applied in spintronics [7–9]. These materials combine a high sensitivity with a remarkable ability to respond to environmental stimuli. Among these, the coexistence of at least two of the three features, ferroelectricity, ferromagnetism, and ferro elasticity due to the interaction of spin, charge, lattice, and orbital degrees of freedom, makes multiferroic materials an attractive option. The magnetoelectric effect, or coupling between electric and magnetic order parameters in multiferroic and magnetoelectric materials, offers an alternate method of controlling the magnetism electrically or the magnetic properties of dielectric materials. Numerous applications of the magnetoelectric effect have been proposed, such as modulators [10], field sensors, energy and frequency converters [11], transformers and gyrators, transducers and memory devices [12], signal amplifiers [13]. They have fascinating application possibilities in contemporary electronics and information technology, particularly in electromagnetic sensors and magnetic storage media. The development, performance enhancement, and use of multiferroic materials have emerged as critical areas of study for strongly correlated electronic systems and spintronics [14].

A half-metallic compound exhibits the behavior of an insulator or semiconductor in one spin channel and that of a metal [15,16]. De Groot et al. introduced the idea of half-metallic compounds. This hybrid activity culminates in complete (100%) spin polarization at the Fermi level. Subsequently, these substances generate spin-polarized current, enhancing magneto-electronic device efficiency. Numerous materials have been proven to be half-metals, including transition



metal pnictides and metal-chalcogenides [17] oxides [18,19], Heusler alloys [20], graphene nanoribbons [21], spinel ferrites [22], zinc-blende [23] and magnetic semiconductors. In the field of spintronics, these magnetic materials have found significant applications [24]. However, more research needs to be done on half-metallicity signatures in multiferroic materials.  $ABO_3$ -type materials are extensively studied for various technological applications such as ferroelectric devices, gas sensors, and actuators—due to their ability to exhibit diverse physical and chemical properties, which depend on the specific metal atoms present at the A and B positions [25].  $BiFeO_3$ , the most well-known compound multiferroic domain, has drawn much attention in recent decades due to its multiferroic characteristics. Examples of multiferroic (MF) materials include  $BiFeO_3$  (BFO), which exhibits a remarkable combination of electronic, optical, magnetic, and ferroelectric properties, and can be readily synthesized via epitaxial growth on  $SrTiO_3$  substrates. Other notable MF compounds are  $YMnO_3$ ,  $BiMnO_3$ ,  $PbNiO_3$ ,  $FeTiO_3$ ,  $PbVO_3$ ,  $YMnO_3$ ,  $TbMn_2O_5$ ,  $Ca_3CoMnO_6$ ,  $LuFe_2O_4$ ,  $BaNiF_4$  among others [26–32]. Soumyasree Jena et al. [33] investigated  $BiFeO_3$  using DFT-based first-principal calculations using the pseudopotential method implemented in the Quantum Espresso (QE) package. They reported the tetragonal phase goes through a half-metallic phase before evolving from a ferromagnetic semiconductor to a ferromagnetic metal as the  $c/a$  ratio drops from 1.264 to 1.016. The half-metallic phase in  $X=B/C/N/F$ -doped  $KNbO_3$  was explored by Rafia Anar and S Nazir et al. [34]. They also looked into the band gap and estimated the Curie temperature in magnetically doped structures using the Heisenberg 2D Hamiltonian model, and they discovered that the temperature was high enough to be useful in practical purposes. Fang et al. [35] investigated the magnetic properties of  $BaMnO_3(Ba_{\frac{1}{3}}Sr_{\frac{1}{3}}Ca_{\frac{1}{3}})TiO_3$  and reported the existence of half-metallic properties using density functional theory. Using the LSDA+U scheme, Zhu et al. [36] the half-metallic nature of the cubic  $BaCrO_3$  structure and show the  $BaCrO_3$  superlattice is a more stable interface than  $BaCrO_3$ . Vinay Sharma and Ram Krishna Ghosh et al. [37] conducted an experimental study on bismuth ferrite ( $BiFeO_3$ ) and confirmed its ferromagnetic nature using X-ray photoelectron spectroscopy (XPS). Their findings were also validated by density functional theory (DFT+U), confirming that this material is feasible for spintronics applications. Recent studies on multiferroic (MF) materials have largely concentrated on modification strategies such as doping, co-doping, heterojunction engineering, the development of double-perovskite structures, and the tuning of intrinsic properties. In addition to these approaches, both experimental and theoretical efforts have been directed toward understanding



key physical characteristics, including optical, vibrational, and elastic behavior. Among the theoretical methods, computational chemistry particularly Density Functional Theory (DFT) has proven to be a highly effective tool, offering a favorable balance between computational cost and predictive accuracy [26,27]. DFT, which is grounded in the Kohn-Sham formalism and incorporates the Exchange-Correlation functional, enables accurate modeling of the electronic structure and related properties. In this work, the B3LYP hybrid functional has been adopted due to its demonstrated reliability and flexibility in the study of complex oxide systems.

The best of our knowledge, there has been no prior theoretical or experimental investigation on the physical properties  $\text{ACrO}_3$  ( $A = \text{Si, Ge, Sn}$ ) multiferroic compounds. Understanding these materials is important, as multiferroics with tunable properties are of great interest for advanced electronic and spintronic applications. Our work aims to fill this gap by systematically investigating and comparing the structural, mechanical, electronic, and optical properties of  $\text{ACrO}_3$  ( $A = \text{Si, Ge, Sn}$ ) compounds under ambient and high-pressure conditions (up to 30 GPa). Such pressure-dependent studies can reveal important insights into the band gap behavior and Curie temperature evolution, which are crucial for designing materials that function reliably at higher temperatures. Therefore, this study provides both a novel theoretical foundation and potential practical implications for the design of future multifunctional devices, particularly in the areas of spintronics and high-pressure electronics.

## 2. Computational Details

The DFT-based CASTEP computer software with the generalized gradient approximation (GGA) has been used for first-principles calculations. The Perdew-Burke-Ernzerhof (PBE) exchange-correlation functional with projected augmented-wave (PAW) pseudopotentials was selected for this calculation [38–40]. In this calculation O- $2s^2 2p^4$ , Cr- $3s^2 3p^6 3d^5 4s^1$  Si- $3s^2 3p^2$ , Ge- $3d^{10} 4s^2 4p^2$ , and Sn- $4d^{10} 5s^2 5p^2$  were used as valance electrons. In the calculation of lattice optimization, the convergence parameters were set as follows: (i) the maximum ionic displacement  $0.002 \text{ \AA}$ , (ii) the maximum stress component  $0.10 \text{ GPa}$ , (iii)  $0.05 \text{ eV/\AA}$  is set for the maximum ionic force. The electromagnetic wave function extension in a plane-wave basis set uses an energy cut-off of  $400 \text{ eV}$ , and the Brillouin zone is sampled using  $8 \times 8 \times 8$  k-points for all calculations. The application of the Broyden has optimized the geometric structure using the Fletcher–Goldfarb–



Shanno (BFGS) minimization technique [41]. The Vanderbilt-type ultrasoft pseudopotential (UPP) formalism was used to analyze the interactions between valence electrons and ions. UPPs achieve a substantially softer pseudo-wave function, requiring a significant reduction in plane waves for calculations with the same level of precision [42]. Additionally, spin polarization was only applied to the magnetic state material in the comparison material used in the lowest energy computation, and spin polarization was not applied to the non-magnetic state material in all other computations. The elastic constants were determined using first-principles computations by carrying out a sequence of specified homogeneous distortions with finite parameters and calculating the resulting stress concerning optimizing the interior atomic freedom. With an upper limit of 0.5%, each strain element had three positive and three negative amplitudes. After that, the calculated stress as a function of strain was fitted linearly to obtain the parameters of the elastic modulus. To facilitate the calculation of the optical properties for a dense mesh of evenly distributed k-points, the BZ integration was performed using a  $12 \times 12 \times 12$  MP k-mesh.

### 3. Results and Discussion

#### 3.1 Ground State Structural Features

$\text{ACrO}_3$  ( $A = \text{Si, Ge, Sn}$ ) is structured in the cubic  $\text{Pm}\bar{3}\text{m}$  space group shown in Figure 1. These structures are optimized in ferromagnetic (FM) and non-magnetic (NM) states to verify the most stable state. All the investigated compounds show more stable in ferromagnetic state from the data reported in Table 1.

To investigate how pressure affects the crystal structure of  $\text{ACrO}_3$  ( $A = \text{Si, Ge, Sn}$ ), we examined the variation in unit cell volume and lattice constant under pressures ranging from 0 to 30 GPa. The results in Figure 2 (a)–(b) indicate that the lattice constant and volume decrease as pressure increases, although they do not decrease at the same rate. As pressure increases, the ratio of  $a/a_0$  and the normalized volume  $V/V_0$ , where  $V_0$  and  $a_0$  stand for the volume at zero pressure, and the equilibrium lattice parameter decreases, as shown in Figure 2(c). This normalization allows for a more precise comparison of how much the lattice parameter and volume change with pressure. Overall, Figure 2 provides a comprehensive view of how  $\text{ACrO}_3$  ( $A = \text{Si, Ge, Sn}$ ) responds to applied pressure, confirming that the material retains its cubic phase while exhibiting significant changes in its structural parameters.





Further we have calculated the cohesive energy ( $E_{\text{coh}}$ ) of  $\text{ABO}_3$  compounds explore more about their structure stability using equations [43],

$$E_{\text{Coh}} = \left[ E_{\text{A}}^{\text{iso}} + E_{\text{B}(\text{Cr})}^{\text{iso}} + 3E_{\text{O}}^{\text{iso}} \right] - E_{\text{ABO}_3}^{\text{Total}} \quad (1)$$

Where  $E_{\text{ABO}_3}^{\text{Total}}$  is the equilibrium total energy of  $\text{ABO}_3$  and  $E_{\text{A}}^{\text{iso}}$ ,  $E_{\text{B}(\text{Cr})}^{\text{iso}}$  and  $E_{\text{O}}^{\text{iso}}$  are the total energies of isolated atoms respectively.

A material with high cohesive energy is more stable due to stronger bonds (e.g., ionic, covalent) that require more energy to break. High cohesive energy correlates with greater hardness, strength, and resistance to deformation, as well as tightly bound electrons that influence conductivity and electronic properties. These results suggest that pressure has a non-linear effect on the cohesive energy of  $\text{ACrO}_3$  ( $\text{A} = \text{Si, Ge, Sn}$ ) compounds. The initial reduction in cohesive energy under pressure could be due to increased repulsion or distortion in the lattice. The slight recovery at higher pressures may indicate a more compact or stabilized structure. All of our compounds possess higher cohesive energy so we can imply that these materials are more resistant to mechanical stress and chemical corrosion, making them suitable for harsh environments.

### 3.2. Bonding analysis

The atomic charges, chemical bond lengths, and bond populations determined using the Mulliken technique are displayed in Table 3. About the nearby O atoms, the charge transfer from  $\text{A} (= \text{Si, Ge, Sn})$  and Cr atoms is around 0.90, 1.22, 1.06 and 0.94 electrons, respectively. The minimal and maximum values for the bond populations suggest that the chemical bond has strong ionicity and covalency, respectively [44,45]. Consequently, we conclude that  $\text{A} (= \text{Si, Ge, Sn})\text{CrO}_3$  exhibits covalent and ionic bonding behavior. Table -3 displays the predicted bond lengths between the various atoms of  $\text{O-A} (= \text{Si, Ge, Sn})$  and  $\text{Cr-O}$  by Mulliken population analysis. A multiferroic compound tolerance factor can be determined by measuring the bond lengths between its constituent atoms, which allows for the identification of the crystal symmetry given by [46],

$$t = \frac{0.707(\text{A} - \text{O})}{(\text{Cr} - \text{O})} \quad (2)$$

Where  $(\text{A-O})$  and  $(\text{Cr-O})$  are bond lengths of  $\text{A} (= \text{Si, Ge, Sn})$  and Cr with O in equation (2). The computed tolerance factor is 0.97, 1.009, and 0.999 for  $\text{SiCrO}_3$ ,  $\text{GeCrO}_3$ , and  $\text{SnCrO}_3$  compounds.



Here are compounds that fall within the range (0.93-1.02) [47], which validates that the compounds are cubic.

### 3.3. Electronics Properties

A thorough understanding of a material's electronic structure is essential for determining its potential applications across various fields of scientific research. The energy band gap, in particular, plays a key role in defining the suitability of a material for use in smart devices, spintronics, and memory technologies. Furthermore, theoretical quantum-level analyses provide a detailed insight into the electronic nature of materials. Based on their electronic properties, materials can be broadly classified as metals, insulators, semiconductors, spin-gapless semiconductors, half-metals, and more [48]. The electronic property of the material is determined by the contributions of various electronic states in the valence and conduction bands. Understanding the electrical structure is crucial for providing helpful information regarding their experimental modeling and potential use in fabricating numerous energy devices. A great deal of individuals believes that GGA typically underestimates the electronic band gap, especially in the case of semiconductors and insulators. This discrepancy is primarily explained by the GGA functional's simplicity and lack of the necessary flexibility to precisely capture exchange-correlation energy, which results in a comparatively lower electronic band gap energy value. So we studied band structure, DOS and PDOS using GGA+U functional [49]. The electrical band structures of  $\text{ACrO}_3$  ( $A = \text{Si, Ge, Sn}$ ) at varying pressures are shown in Figure 3. Figure 3 indicates that the top of the valence band (VB) and bottom of the conduction band (CB) do not overlap, where the top of VB and bottom of CB occur at the R symmetry point. This suggests that the  $A$  ( $= \text{Si, Ge, Sn}$ ) $\text{CrO}_3$  compound exhibits half-metallic behavior.

It has been discovered that in ambient conditions, the top of the (VB) and the bottom of the (CB) are located at the R symmetry point. Remarkably, it was found that for the  $\text{SnCrO}_3$  compound, elevating the pressure caused the VB top at R and  $\Gamma$  symmetry locations to move closer to the Fermi level and at 20 and 30 GPa top of the valence band at R and  $\Gamma$  symmetry points cross the Fermi level. On the other hand, no relative shift has been seen when looking at the band structure of  $\text{SiCrO}_3$  and  $\text{GeCrO}_3$  compounds, suggesting that these materials' electrical characteristics stay stable under external pressure. Due to this, band structure stability,  $\text{SiCrO}_3$  and  $\text{GeCrO}_3$  may retain





consistent electrical conductivity and other electronic properties. When closely examined, Figure 3 energy band edges at the R and  $\Gamma$  points have flat bands, while the remaining points exhibit slightly bouncy curvature. This indicates that  $\text{ACrO}_3$  ( $A = \text{Si, Ge, Sn}$ ) has higher effective masses at the L and  $\Gamma$  points than at other locations [50].

The spin-polarized total and partial density of states (DOSs), displayed in Figure 5 and 6, explain various electronic states' contributions to the band structure. When considering the up-spin channel, the  $\text{ACrO}_3$  ( $A = \text{Si, Ge, Sn}$ ) compounds possess occupied states at the Fermi level and show metallic characteristics. On the other hand,  $\text{ACrO}_3$  ( $A = \text{Si, Ge, Sn}$ ) exhibits semiconducting behavior for the down-spin channel and unoccupied states at the Fermi level. Figure 5 shows that as pressure is increased to 30 GPa, conduction bands move downward, valance bands shift upward, and the band gap eventually contracts for  $\text{SiCrO}_3$  and  $\text{SnCrO}_3$ . Figure-5 indicates that at pressures of 30 Gpa, there is no band gap at the Fermi level, and the material exhibits metallic behavior. Thus, we state that the  $\text{SiCrO}_3$  and  $\text{SnCrO}_3$  a compound undergoes a phase shift at 30 GPa. The semiconducting gap in  $\text{GeCrO}_3$  compounds is almost constant throughout the pressure range, suggesting that the electronic bandgap is highly stable and is not affected by variations in pressure.

Figure 6 clearly shows that in the spin-up channel, the O-2p state contributes to the bottom of the valance band (VB) at -2.4 eV, while the Cr-3d state at the Fermi level significantly contributes. The plot indicates that the hybridization of O-2p and Cr-3d states is responsible for the top of the valence band and that this hybridization contributes more to the spin-up channel than the spin-down channel, making the  $\text{ACrO}_3$  ( $A = \text{Si, Ge, Sn}$ ) compounds metallic in spin up-channel. Interestingly, the O-2p state at the bottom of the valance band drifts leftwards with increasing pressure. In the conduction of the band, the highest contribution comes from the Sn-s state at 2.2eV and the O-2p state at 4.5eV. In the case of a down channel, polarization occurs at the Fermi level, and the 3d state of the Cr atom jumps into the conduction band and is localized at 2.2eV.

### 3.4. Spin magnetic moment and spin polarization

The temperature at which spontaneous magnetization in magnetic material ceases is called the curie temperature, sometimes referred to as the curie point or the magnetic transition point. Using Heisenberg mean field approximation [51],



$$T_C = \frac{\Delta E}{3K_B} \quad (3)$$

Where  $\Delta E$  is the energy difference between non-magnetic  $E_{NM}$  and ferromagnetic state  $E_{FM}$  and represents the energy barrier that must be overcome to transition from the non-magnetic to the ferromagnetic state. Figure-7 illustrates the Curie temperature did not fall linearly on pressure but rapidly decreased, especially  $\text{SiCrO}_3$ , which fell quickly relative to the rest of the investigated compounds. J.M. Leger et al. [52] investigated the pressure effect on  $T_C$  of alloy with transition atom and found similar trends, which make our result consistent with the literature. We found that the Curie temperature at normal pressure is 1236.71K, 772.94K, and 1082.12K for  $\text{ACrO}_3$  ( $A = \text{Si, Ge, Sn}$ ) compounds, which is relatively higher than room temperature and only seen in full-Heusler alloy [53].  $\text{ACrO}_3$  ( $A = \text{Si, Ge, Sn}$ ) has a high Curie temperature, making it a promising material for spintronics applications [54].

At  $T = 0 \text{ K}$ , the spin-polarized computation directly obtains the magnetic moment. Utilizing the actual magnetic moments per formula unit, the magnetic moment is calculated as follows,

$$\mu = 3\mu_{\text{oxygen}} + \mu_{\text{Cr}} + \mu_{\text{A(Sn, Ge, Si)}} \quad (4)$$

The calculated magnetic moment is listed in Table 3, and it is observed that the pressure is up to 10-GPa, and the total magnetic moment is almost the same for all the compounds but after 10 GPa in the compounds  $\text{SnCrO}_3$ , the total magnetic moment changed. Additionally, we looked into how pressure affected each of the three compounds' magnetic moments per atom between 0 and 30 GPa. To our knowledge, MOULAY et al. [55] investigation on the pressure dependence of magnetic moments for multiferroic compounds revealed that the individual elements' magnetic moments do not significantly change in response to pressure.

The constant compression of its lattice directly impacts the physical characteristics of a material. These characteristics influence the compound's magnetic, structural, electrical, and optical qualities. The robust shift lattice parameter (RTLCP) is the critical lattice parameter at which the total magnetic moment of a half-metal substance abruptly shifts to a non-integer value, and the electronic nature of the compound changes from half-metal to metal at that lattice parameter, making it a fundamental lattice constant to study [56]. Figure 9 shows that the  $\text{SnCrO}_3$  compound magnetic moment changed from an integer ( $\cong 1.99 \mu_B$ ) to a non-integer value as the lattice constant decreased with an increase in external pressure. At  $3.78 \text{ \AA}$ , there is a sudden transition and the



compound loses its integer magnetic moment ( $2\mu_B$  to  $0.50\mu_B$ ). This sudden shift verifies that the  $\text{SnCrO}_3$  compound robust lattice is  $3.78 \text{ \AA}$ .

The spin polarization of  $\text{ACrO}_3$  ( $A = \text{Si, Ge, Sn}$ ) is reflected by the bandgap present at the Fermi level, which is essentially the difference in spin density between the spin up and down channels near the Fermi level ( $E_F$ ). Spin polarization can be obtained from the following relation,

$$\text{Spin} - \text{polarization} = \frac{N\uparrow(E_F) - N\downarrow(E_F)}{N\uparrow(E_F) + N\downarrow(E_F)} \quad (5)$$

$N\uparrow(E_F)$  and  $N\downarrow(E_F)$  are the density of states at spin-up and spin-down channels near the Fermi level. Among these two channels, when any of the states of the Fermi level is zero, 100% spin polarization will occur. From the band diagram, the density of state figure, it is observed that the density of state along the down channel near the Fermi level is zero, which makes  $\text{ACrO}_3$  ( $A = \text{Si, Ge, Sn}$ ) a half-metallic material.

### 3.5. Mechanical properties

Elastic constants are necessary to have a more thorough theoretical comprehension of the characteristics of materials that are determined by the electron-phonon interaction processes and the density of states of phonons. Since the stress-strain curve in many minerals exhibits low nonlinearity, practical applications can assume a linear relationship between stress and strain [57]. Elastic constants can calculate essential physical parameters like melting point, hardness, sound velocities, Debye temperature, and shear modulus. The elastic constants are the total energy second derivative for different lattice deformations. More thorough computations of the total energy are necessary [58] for the elastic constants. The elastic constants can be calculated from the resulting formula,

$$C_{ij} = \frac{1}{V_0} \left( \frac{d^2 E}{de_i de_j} \right) \quad (6)$$

$E$  is the internal energy,  $V_0$  indicate equilibrium volume and  $e_i$  and  $e_j$  is the stress and strain components.

Since  $\text{ACrO}_3$  ( $A = \text{Si, Ge, Sn}$ ) is a cubic structure with a high degree of symmetry, the elastic constant reduces to three independent elastic constants:  $C_{11}$ ,  $C_{12}$ , and  $C_{44}$  [59]. The following is an



expression of the conventional mechanical stability conditions in cubic crystals at equilibrium in terms of elastic constants [60,61],

$$C_{44} > 0, C_{11} > |C_{12}|, C_{11} + 2C_{12} > 0 \quad (7)$$

The equations for mechanical stability under pressure are given by [62],

$$C'_{11} - C'_{12} = (C_{11} - C_{12}) - 2P > 0, C'_{11} + 2C'_{12} = (C_{11} + 2C_{12}) - 2P > 0, C'_{44} = C_{44} - P > 0 \quad (8)$$

From the data reported in Table 5 the dynamical stability of the compounds  $ACrO_3$  ( $A = Si, Ge, Sn$ ) was assessed using pressure-modified elastic criteria.  $SiCrO_3$  and  $SnCrO_3$  are dynamically stable at 0, 10, and 30 GPa, but both exhibit instability at 20 GPa, primarily due to a negative  $C_{44} - P$ , indicating shear softening under pressure. In contrast,  $GeCrO_3$  is unstable at ambient pressure but becomes dynamically stable at pressures above 10 GPa, suggesting pressure-induced stabilization. The formulations associated with the calculations of Bulk modulus( $B$ ), Shearing modulus( $G$ ), Young's modulus( $E$ ), Anisotropy( $A$ ), Poisson's ratio( $\nu$ ), Pugh's ratio( $B/G$ ), plasticity measurement( $B/C_{44}$ ), Kleinman parameter ( $\zeta$ ) have been computed using the following are given by the following expressions, respectively [63–67],

$$B = \frac{1}{3}(C_{11} + 2C_{12}) \quad (9)$$

$$G = \frac{G_V + G_R}{2} \quad (10)$$

$$G_V = \frac{C_{11} - C_{12} + C_{44}}{5} \quad (11)$$

$$G_R = \frac{5C_{44}(C_{11} - C_{12})}{4C_{44} + 3(C_{11} - C_{12})} \quad (12)$$

$$E = \frac{9BG}{(3B + G)} \quad (13)$$

$$A = \frac{2C_{44}}{C_{11} - C_{12}} \quad (14)$$

$$\nu = \frac{(3B - 2G)}{2(3B + G)} \quad (15)$$

$$\zeta = \frac{C_{11} + 8C_{12}}{7C_{11} + 2C_{12}} \quad (16)$$



Since the shear modulus indicates the rigidity of a compound rather than the bulk modulus, the mechanical failure in  $ACrO_3$  ( $A = Si, Ge, Sn$ ) should be revealed by the shear component under the criteria  $G < B$  in this case. The bulk modulus of a material determines the counteraction against the volume change due to applied pressure, compared to the shear modulus, which defines the counteraction against plastic distortion [68]. The bulk modulus values of  $SiCrO_3$ ,  $GeCrO_3$  and  $SnCrO_3$  exhibit a clear increasing trend with applied pressure, indicating enhanced resistance to volume compression. For  $SiCrO_3$ , the bulk modulus increases from 674.13 GPa at 0 GPa to 840.77 GPa at 30 GPa, suggesting improved mechanical rigidity under compression.  $GeCrO_3$  shows a substantial increase from 185.12 GPa to 852.15 GPa over the same pressure range, which may indicate a pressure-induced structural stabilization. In the case of  $SnCrO_3$ , the bulk modulus rises steadily from 616.97 GPa to 840.77 GPa, reflecting consistent stiffening behavior under pressure. A solid stiffness can be determined by calculating its Young's modulus ( $E$ ), which is the ratio of tensile stress to tensile strain, and a low value of  $E$  indicates more remarkable plasticity. In the current investigation, the compound's Young modulus ( $E$ ) for  $GrCrO_3$  and  $SnCrO_3$  is relatively low at 0 and 10 GPa and significantly loses flexibility at higher pressures. On the other hand,  $SiCrO_3$  has a maximum value at pressure 10GPa compared to other applied pressures.

Poisson's ratio, an elastic constant that describes how a material deforms sideways in response to longitudinal force, is also known as the transverse deformation coefficient. Poisson's ratio is a characteristic with a minimum value of approximately 0.25 [69] in most metals. We may infer the ductile or brittle behaviors of  $GeCrO_3$ ,  $SiCrO_3$ , and  $SnCrO_3$  under various pressure situations from Figure-11. The graphic illustrates how each compound responds differently to pressure variations overall, all the compounds exhibit ductile nature under whole pressure range. The decreasing trend of Poisson's ratio in  $GeCrO_3$  under pressure may suggest a transition toward a more brittle nature, which could be due to pressure-induced changes in bonding or structure.

The distortion of a material (solid) that experiences irreversible shape changes in response to an applied force is called plasticity in material science [70]. The link between applied pressure and the plasticity of the compounds  $SiCrO_3$ ,  $GeCrO_3$ , and  $SnCrO_3$  is depicted in Figure 10(b). The plasticity of  $SiCrO_3$ ,  $GeCrO_3$  and  $SnCrO_3$  exhibits a clear dependence on applied pressure, reflecting changes in their mechanical response under stress. For  $SiCrO_3$ , plasticity increases from 11.07 at 0 GPa to 14.93 at 30 GPa, indicating improved capacity for permanent deformation.  $GeCr$



O<sub>3</sub> initially shows low plasticity (2.47 at 0 GPa), which rises steadily to 9.86 at 30 GPa, suggesting pressure-induced enhancement in ductility likely due to changes in bonding or structural arrangement. SnCrO<sub>3</sub> follows a similar trend, with plasticity increasing from 4.87 to 14.93 over the same pressure range, pointing to significant improvement in deformability under compression. These trends highlight the potential of these materials for high-pressure applications where mechanical adaptability is critical [71].

Anisotropy is a crucial compound parameter for engineering science applications. When a material's anisotropy value is precisely unity, it is considered isotropic, and any other value indicates the degree of elastic anisotropy that the crystal possesses. The value of parameter A for the compounds ACrO<sub>3</sub> (A = Si, Ge, Sn) exhibits a behavior that is either less than or higher than unity, making the crystal anisotropic.

### 3.6. Optical Properties

Knowing a material's optical characteristics is essential to figuring out its optoelectronic nature. Furthermore, examining optical properties is crucial because semiconductors frequently display metal-like activity at extremely low frequencies and insulating behavior at very high frequencies [72]. Figure-10(a)-(b) displays the computed  $\epsilon_1(\omega)$  and  $\epsilon_2(\omega)$  components of the dielectric function under the pressure of 0-30 GPa in the 0-30 eV range for ACrO<sub>3</sub> (A = Si, Ge, Sn) with electric field polarization vectors along [100] direction. As the resulting photon energy raised in the low energy zone, the dielectric functions (both real part  $\epsilon_1$  and imaginary part  $\epsilon_2$ ) were significantly lowered, as Figure 13(a) illustrates. The observed dielectric constant trend suggests that the compound under investigation is appropriate for use in microelectronic applications and integrated circuits [73]. The dielectric function is a complex function which is given by [74],

$$\epsilon(\omega) = \epsilon_1(\omega) + i\epsilon_2(\omega) \quad (17)$$

One of the key properties of half-metallic material known as plasma frequency  $\omega_p$ . It has a real component of dielectric function with zero value [74]. Based on Figure-12(a), we can see that SiCrO<sub>3</sub> and GeCrO<sub>3</sub> compounds has zero value of  $\epsilon_1$  in the entire pressure range in the ultraviolet region 5-10 eV. In contrast, SnCrO<sub>3</sub> also have zero value in the visible energy range for 10-30 GPa and at pressures of 0 and 20 GPa in the ultraviolet region where transitions occur from metallic to





dielectric. At the IR spectrum region, the real component of the dielectric function shows a distinctive peak. The intra-band Drude-like characteristic of  $ACrO_3$  ( $A = Si, Ge, Sn$ ) is the negative frequency of the real part of the dielectric function. The imaginary part of the dielectric function has a value that is immensely close to zero, and the real part tends to be united in the high-energy zone. It verifies that the material is optically isotropic by presenting it as a virtually transparent substance with minimal absorption in the infrared spectrum. The static dielectric constant  $\epsilon_1(0)$  at pressure 0, 10, 20 and 30 GPa are 0.5, 5 and 5.5 eV for  $SnCrO_3$ . It is evident from Figures-12(a)–(b) that the real and imaginary components of the dielectric functions both have relatively greater values at low energies and begin to decline as energy increases.

Refractive index  $n(\omega)$  is a crucial optical characteristic that may be found in terms of the complex dielectric function as shown in [75],

$$n(\omega) = \frac{1}{\sqrt{2}} \left( \epsilon_1 + (\epsilon_1^2 + \epsilon_2^2)^{\frac{1}{2}} \right)^{1/2} \quad (18)$$

The spectrum of refractive index with incident energy is displayed in Figure-12(c). The mechanism of free electrons in metallic compounds is responsible for the maximum value of the  $A$  ( $= Si, Ge, Sn$ ) $CrO_3$  refractive index at low energy regions. For compounds  $SiCrO_3$  and  $GeCrO_3$ , the refractive index has significant peaks in the visible energy range, is approximately constant for the whole pressure range, and gradually drops in the ultraviolet energy region.  $SnCrO_3$  has refractive index peaks in the infrared and progressively drops in the visible and ultraviolet wavelength ranges.

Optical conductivity  $\sigma(\omega)$  of  $ACrO_3$  ( $A = Si, Ge, Sn$ ) demonstrated in Figure-13(d). It is an important optical parameter that may be expressed as follows:

$$\sigma(\omega) = \frac{W_{cv} \hbar}{\pi E_0^2} \quad (19)$$

Where  $W_{cv}$  is the transition probability per unit of time [76]. From Figure 12-d shows that for  $SiCrO_3$  and  $GeCrO_3$ , conductivity increases quickly in the visible energy zone and reaches its maximum value in the ultraviolet range as incident energy increases.  $SiCrO_3$  and  $GeCrO_3$  have the highest conductivity among these compounds at 20 GPa, with no peaks seen in the visible or infrared spectrum.  $SnCrO_3$  spectra differ significantly from the other compounds, with two minor peaks



occurring in the energy ranges of 4.8-7.5 eV and 1-2.5 eV. In the second significant peak, the conductivity in the ultraviolet energy region increases as pressure rises. Because of the hybridization of the valence and conduction bands, conductivity begins at zero photon energy, indicating that there is no band gap at the Fermi level for the up channel, which was confirmed during the investigation of the density of the state.

ACrO<sub>3</sub> (A = Si, Ge, Sn) compounds absorption coefficient  $I(\omega)$  spectra are shown in Figure-12(e). This spectrum gives information on light absorption and the final disappearance of an incident electromagnetic beam that passes through an absorbing material. In the infrared region, at 0 and 30 GPa pressures, compounds ACrO<sub>3</sub> (A = Si, Ge, Sn) absorb incident light and show semiconducting characteristics. When pressure increases, the first noticeable peaks for SiCrO<sub>3</sub> and GeCrO<sub>3</sub> compounds are seen in the 6–9 eV energy range. These peaks move to the right with increasing pressure. SnCrO<sub>3</sub> compounds, on the other hand, have a modest peak in the infrared region and reach their most significant value in the ultraviolet. ACrO<sub>3</sub> (A = Si, Ge, Sn) showed recurrent peaks in the 10–20 eV energy region. The absorption edge was altered as a pressure function because of the decrease in the band gap. Our analysis shows that SnCrO<sub>3</sub> has an excellent absorption coefficient in the high energy range, with the most prominent peaks occurring at 27.5 eV.

Reflectivity is the ratio of incident power to reflected power describes a material surface characteristic and is calculated using following equation [77],

$$R(\omega) = \left| \frac{\sqrt{\epsilon(\omega)} - 1}{\sqrt{\epsilon(\omega)} + 1} \right|^2 \quad (20)$$

Figure 12 (f) demonstrates that reflectivity as a function of incident energy. SiCrO<sub>3</sub> and GeCrO<sub>3</sub> compounds has reflectances between 40 and 45 percent at zero-incident energy, and their spectra are nearly identical. The reflectivity decreases in the visible energy range before increasing to a high of roughly 48% at 0 GPa and a roughly constant value of 50% between 0 and 30 GPa. For SnCrO<sub>3</sub>, reflectivity starts from 0.51, 0.78 and 0.85 eV for 0, 10, 20 and 30 GPa, respectively, for zero-incident energy. Reflectivity falls significantly with increasing incident energy at 10 and 30 GPa, which drops by about 55%, and at 0 and 10 GPa. It declines by roughly 30% throughout a range of 1.5 eV in the visible energy region, with some minor fluctuations in the 4-7 eV range. In the ultraviolet radiation range, the maximum reflectance is roughly 52% for 0 and 10 GPa and



44% and 46% for 20 and 30 GPa. It is seen that the reflectivity peaks for all the compounds shift to the right, undergoing a significant form change as pressure increases from 0 to 30 GPa. Figure 12 (f) reveals that  $\text{ACrO}_3$  ( $A = \text{Si, Ge, Sn}$ ) is not a good reflector in the visible region, and the  $R(0)$  value is relatively high in the IR region compared to another area. So  $\text{ACrO}_3$  ( $A = \text{Si, Ge, Sn}$ ) can be used in IR mirrors, coating for optical instruments [78]. The loss per unit area resulting from heating, plasma resonance, and scattering is measured by the optical energy loss factor  $L(\omega)$ . The electron energy loss function  $L(\omega)$  can be obtained from the real and imaginary components of the complex dielectric function:

$$L(\omega) = \left( \frac{\epsilon_2(\omega)}{\epsilon_1^2(\omega) + \epsilon_2^2(\omega)} \right) \quad (21)$$

Figure 12 (g) illustrates the electron energy loss spectrum (EELS). We observed negligible energy loss of electrons within  $\text{ACrO}_3$  ( $A = \text{Si, Ge, Sn}$ ) compounds in the IR and visible energy range. The significant losses occur in the ultraviolet energy region in between (25-30eV). Therefore, from energy loss spectra, the significant peaks of plasmon energy (a collective oscillation of valance electron energy) situated at 27, 27.5, 28 and 29eV respectively, at 0, 10, 20, and 30 GPa for  $\text{SnCrO}_3$ , which indicates that the plasmon energy spectrum moves towards higher energy region as pressure rising. Similar features have been observed in  $\text{SiCrO}_3$  and  $\text{GeCrO}_3$  compounds, where major peaks move toward the right with increasing pressure. The highest peak in the energy loss spectrum occurs because of bulk plasmonic excitation. This happens at a specific incident photon energy and its corresponding frequency, known as the bulk plasma frequency [79]. Rather than absorbing high-energy photons, we detected some modest peaks in the energy range of 15-20 eV, which suggest surface plasmonic excitations at the metal-dielectric interface due to optical transition. This loss spectroscopy indicated that the substance might be used for non-linear optics, biosensors, near-field optics (light guiding below the diffraction limit), and other applications [80].

## 4. Conclusion

In this study, we used the DFT framework with a generalized gradient approximation (GGA) to investigate  $\text{ACrO}_3$  ( $A = \text{Si, Ge, Sn}$ ) compounds. Our results were consistent with those reported in the literature. We found that the lattice constant and bond length decrease with increasing



hydrostatic pressure. The investigated substances retained their cubic phases over a range of pressures. Determining the tolerance factor, confirmed the stability of the cubic phase under different pressure regimes.  $\text{ACrO}_3$  ( $A = \text{Si, Ge, Sn}$ ) was found to be a half-metal based on spin-polarized electronic band structures, the density of states, and the integer value of the magnetic moment ( $\mu_B$ ) per unit cell. We observed that the structure is more stable in the ferromagnetic state than in the non-magnetic state. An analysis of Mulliken charges showed that  $\text{ACrO}_3$  ( $A = \text{Si, Ge, Sn}$ ) exhibits covalent and ionic bonding behavior.  $\text{SnCrO}_3$  exhibited metallic behavior at the critical lattice constant after losing its integer magnetic moment, while the other compounds maintained constant magnetic moments. We also examined the ductile and brittle behavior and bonding characteristics of the compounds using Poisson's ratios. Our analysis indicated that  $\text{SiCrO}_3$  and  $\text{SnCrO}_3$  are brittle at 0 and 10 GPa and ductile at other pressure regions, while  $\text{GeCrO}_3$  exhibited ductile behavior at all pressures. The Kleinman parameter decreased linearly, suggesting a decrease in plasticity with pressure. Additionally, we investigated the optical behavior of  $\text{ACrO}_3$  ( $A = \text{Si, Ge, Sn}$ ) by calculating the dielectric function, refractive index, optical conductivity, absorption, reflectivity, and energy loss function. We observed maximum absorption and minimum energy loss in the ultraviolet region. The real and imaginary parts of the dielectric function showed that the compound is metallic in the infrared and visible range, while exhibiting semiconducting behavior in the ultraviolet energy region. Since there is no literature data available for these  $\text{ACrO}_3$  ( $A = \text{Si, Ge, Sn}$ ) materials and the data reported in this study can serve as a reference for future research and will be valuable for understanding and developing effective optoelectronic and spintronics devices.

## Acknowledgements

"We thankfully acknowledge the Ministry of Science and Technology, Bangladesh for their financial support in this project conducted by the members of the Condensed Matter Physics lab at Jahangirnagar University through their R&D fund allocation program." We are also thankful to the Jahangirnagar University-funded Project for the financial assistance to conduct the research work in the Computational Physics (CP) Research Lab in the Department of Physics at Jahangirnagar University.



## Reference

- [1] J. Fabian, A. Matos-Abiague, C. Ertler, P. Stano, I. Zutic, *Semiconductor Spintronics*, *Acta Physica Slovaca* 57 (2007) 659–700. <https://doi.org/10.2478/v10155-010-0086-8>.
- [2] D.D. Awschalom, M.E. Flatté, Challenges for semiconductor spintronics, *Nat Phys* 3 (2007) 153–159. <https://doi.org/10.1038/NPHYS551;KWRD=PHYSICS>.
- [3] V. Baltz, A. Manchon, M. Tsoi, T. Moriyama, T. Ono, Y. Tserkovnyak, Antiferromagnetic spintronics, *Rev Mod Phys* 90 (2018) 015005. <https://doi.org/10.1103/REVMODPHYS.90.015005/FIGURES/48/THUMBNAI>.
- [4] P. Chongthanaphisit, K.J. Lee, S. Lee, X. Liu, M. Dobrowolska, J.K. Furdyna, Gate control of interlayer exchange coupling in ferromagnetic semiconductor trilayers with perpendicular magnetic anisotropy, *APL Mater* 10 (2022). [https://doi.org/10.1063/5.0079245/16489526/041102\\_1\\_ACCEPTED\\_MANUSCRIPT.PDF](https://doi.org/10.1063/5.0079245/16489526/041102_1_ACCEPTED_MANUSCRIPT.PDF).
- [5] R. Lebrun, A. Ross, S.A. Bender, A. Qaiumzadeh, L. Baldrati, J. Cramer, A. Brataas, R.A. Duine, M. Kläui, Tunable long-distance spin transport in a crystalline antiferromagnetic iron oxide, *Nature* 561 (2018) 222–225. <https://doi.org/10.1038/S41586-018-0490-7>.
- [6] X. Yang, Z. Zhou, T. Nan, Y. Gao, G.M. Yang, M. Liu, N.X. Sun, Recent advances in multiferroic oxide heterostructures and devices, *J Mater Chem C Mater* 4 (2015) 234–243. <https://doi.org/10.1039/C5TC03008K>.
- [7] S. Heo, S.K. Sharma, S. Lee, Y. Lee, C. Kim, B. Lee, H. Lee, D.Y. Kim, Effects of y contents on surface, structural, optical, and electrical properties for Y-doped ZnO thin films, *Thin Solid Films* 558 (2014) 27–30. <https://doi.org/10.1016/J.TSF.2014.02.025>.
- [8] S. Baturay, Y.S. Ocak, D. Kaya, The effect of Gd doping on the electrical and photoelectrical properties of Gd:ZnO/p-Si heterojunctions, *J Alloys Compd* 645 (2015) 29–33. <https://doi.org/10.1016/J.JALLCOM.2015.04.212>.
- [9] S. Chen, L. Lin, J. Liu, P. Lv, X. Wu, W. Zheng, Y. Qu, F. Lai, An electrochemical constructed p-Cu<sub>2</sub>O/n-ZnO heterojunction for solar cell, *J Alloys Compd* 644 (2015) 378–382. <https://doi.org/10.1016/J.JALLCOM.2015.02.230>.
- [10] Magnetoelectric Spin Wave Modulator Based On Synthetic Multiferroic Structure. - Abstract - Europe PMC, (n.d.). <https://europepmc.org/article/pmc/pmc6052081> (accessed June 15, 2025).
- [11] S. Sharma, A. Paliwal, M. Tomar, V. Gupta, Multiferroic BFO/BTO multilayer structures based magnetic field sensor, *Physica B Condens Matter* 571 (2019) 1–4. <https://doi.org/10.1016/J.PHYSB.2019.06.056>.
- [12] (PDF) Multiferroic materials for sensors, transducers and memory devices, (n.d.). [https://www.researchgate.net/publication/237010601\\_Multiferroic\\_materials\\_for\\_sensors\\_transducers\\_and\\_memory\\_devices](https://www.researchgate.net/publication/237010601_Multiferroic_materials_for_sensors_transducers_and_memory_devices) (accessed June 15, 2025).
- [13] M.M. Vopson, Fundamentals of multiferroic materials and their possible applications, *Critical Reviews in Solid State and Materials Sciences* 40 (2015) 223–250. <https://doi.org/10.1080/10408436.2014.992584>;
- [14] Z. Zanolli, Graphene-multiferroic interfaces for spintronics applications, *Scientific Reports* 2016 6:1 6 (2016) 1–6. <https://doi.org/10.1038/srep31346>.
- [15] W.E. Pickett, J.S. Moodera, Half Metallic Magnets, *Phys Today* 54 (2001) 39–44. <https://doi.org/10.1063/1.1381101>.



- [16] I. Galanakis, P.H. Dederichs, N. Papanikolaou, Slater-Pauling behavior and origin of the half-metallicity of the full-Heusler alloys, *Phys Rev B* 66 (2002) 174429. <https://doi.org/10.1103/PhysRevB.66.174429>.
- [17] I. Galanakis, P. Mavropoulos, Zinc-blende compounds of transition elements with N, P, As, Sb, S, Se, and Te as half-metallic systems, *Phys Rev B* 67 (2003) 104417. <https://doi.org/10.1103/PhysRevB.67.104417>.
- [18] J. Dho, S. Ki, A.F. Gubkin, J.M.S. Park, E.A. Sherstobitova, A neutron diffraction study of half-metallic ferromagnet CrO<sub>2</sub> nanorods, *Solid State Commun* 150 (2010) 86–90. <https://doi.org/10.1016/J.SSC.2009.09.044>.
- [19] S. Soeya, J. Hayakawa, H. Takahashi, K. Ito, C. Yamamoto, A. Kida, H. Asano, M. Matsui, Development of half-metallic ultrathin Fe<sub>3</sub>O<sub>4</sub> films for spin-transport devices, *Appl Phys Lett* 80 (2002) 823–825. <https://doi.org/10.1063/1.1446995>.
- [20] A. Amudhavalli, R. Rajeswarapalanichamy, K. Iyakutti, Half metallic ferromagnetism in Ni based half Heusler alloys, *Comput Mater Sci* 148 (2018) 87–103. <https://doi.org/10.1016/J.COMMATSCI.2018.02.026>.
- [21] Y.W. Son, M.L. Cohen, S.G. Louie, Half-metallic graphene nanoribbons, *Nature* 444 (2006) 347–349. <https://doi.org/10.1038/NATURE05180>.
- [22] S. Ali, H. Ullah, A.A. AlObaid, T.I. Al-Muhimeed, Crystal field splitting, half metallic ferromagnetism, structural, mechanical and magneto-electronic properties of spinels type structure compounds MgX<sub>2</sub>O<sub>4</sub> (X = Fe and Co) for spintronic applications, *Eur Phys J Plus* 136 (2021). <https://doi.org/10.1140/EPJP/S13360-021-01737-W>.
- [23] B.G. Liu, Robust half-metallic ferromagnetism in zinc-blende CrSb, *Phys Rev B* 67 (2003) 172411. <https://doi.org/10.1103/PhysRevB.67.172411>.
- [24] R.A. De Groot, F.M. Mueller, P.G.V. Engen, K.H.J. Buschow, New Class of Materials: Half-Metallic Ferromagnets, *Phys Rev Lett* 50 (1983) 2024. <https://doi.org/10.1103/PhysRevLett.50.2024>.
- [25] N.A. Benedek, C.J. Fennie, Why are there so few perovskite ferroelectrics?, *Journal of Physical Chemistry C* 117 (2013) 13339–13349. [https://doi.org/10.1021/JP402046T/SUPPL\\_FILE/JP402046T\\_SI\\_001.PDF](https://doi.org/10.1021/JP402046T/SUPPL_FILE/JP402046T_SI_001.PDF).
- [26] C.J. Fennie, Ferroelectrically Induced Weak Ferromagnetism by Design, *Phys Rev Lett* 100 (2008) 167203. <https://doi.org/10.1103/PHYSREVLETT.100.167203/FIGURES/3/THUMBNAI>.
- [27] I.A. Sergienko, E. Dagotto, Role of the Dzyaloshinskii-Moriya interaction in multiferroic perovskites, *Phys Rev B Condens Matter Mater Phys* 73 (2006) 094434. <https://doi.org/10.1103/PHYSREVB.73.094434/FIGURES/5/THUMBNAI>.
- [28] T. Moriya, Anisotropic Superexchange Interaction and Weak Ferromagnetism, *Physical Review* 120 (1960) 91. <https://doi.org/10.1103/PhysRev.120.91>.
- [29] I. Dzyaloshinsky, A thermodynamic theory of “weak” ferromagnetism of antiferromagnetics, *Journal of Physics and Chemistry of Solids* 4 (1958) 241–255. [https://doi.org/10.1016/0022-3697\(58\)90076-3](https://doi.org/10.1016/0022-3697(58)90076-3).
- [30] S. Esposito, A. Naddeo, The Genesis of the Quantum Theory of the Chemical Bond, *Advances in Historical Studies* 03 (2014) 229–257. <https://doi.org/10.4236/AHS.2014.35020>.
- [31] J.B. Goodenough, J. Zhou, Varied roles of Pb in transition-metal PbMO<sub>3</sub> perovskites (M = Ti, V, Cr, Mn, Fe, Ni, Ru), *Sci Technol Adv Mater* 16 (2015). <https://doi.org/10.1088/1468-6996/16/3/036003>.





- [32] L.H. da S. Lacerda, S.R. de Lazaro, Multiferroism and magnetic ordering in new  $\text{NiBO}_3$  ( $B = \text{Ti, Ge, Zr, Sn, Hf}$  and  $\text{Pb}$ ) materials: A DFT study, *J Magn Magn Mater* 465 (2018) 412–420. <https://doi.org/10.1016/J.JMMM.2018.06.029>.
- [33] S. Jena, S. Bhattacharya, S. Datta, Signature of half-metallicity in  $\text{BiFeO}_3$ : A DFT study, *Comput Mater Sci* 204 (2022) 111107. <https://doi.org/10.1016/J.COMMATSCI.2021.111107>.
- [34] R. Anar, S. Nazir, Exploring multiferroicity, half-metallic phase, and curie temperature in  $X = \text{B/C/N/F}$ -Doped  $\text{KNbO}_3$ : a DFT aspect, *Phys Scr* 99 (2024). <https://doi.org/10.1088/1402-4896/AD21C8>.
- [35] S. Yoon, K. Son, S.G. Ebbinghaus, M. Widenmeyer, A. Weidenkaff, Ferromagnetism in nitrogen and fluorine substituted  $\text{BaTiO}_3$ , *J Alloys Compd* 749 (2018) 628–633. <https://doi.org/10.1016/J.JALLCOM.2018.03.221>.
- [36] Z.H. Zhu, X.H. Yan, Half-metallic properties of perovskite  $\text{BaCrO}_3$  and  $\text{BaCr}_{0.5}\text{Ti}_{0.5}\text{O}_3$  superlattice: LSDA+U calculations, *J Appl Phys* 106 (2009). <https://doi.org/10.1063/1.3182721/393660>.
- [37] M. tariq, A. Shaari, K. Chaudhary, R. Ahmed, M.A. Jalilj, F.D. Ismail, Magnetoelectric, and Dielectric Switching Properties of Co-Doped  $\text{BiFeO}_3$  for Low Energy Memory Technology: A First-Principles Study, *SSRN Electronic Journal* (2022). <https://doi.org/10.2139/SSRN.4223051>.
- [38] J.P. Perdew, A. Zunger, Self-interaction correction to density-functional approximations for many-electron systems, *Phys Rev B* 23 (1981) 5048. <https://doi.org/10.1103/PhysRevB.23.5048>.
- [39] D.M. Ceperley, B.J. Alder, Ground State of the Electron Gas by a Stochastic Method, *Phys Rev Lett* 45 (1980) 566. <https://doi.org/10.1103/PhysRevLett.45.566>.
- [40] M.D. Segall, P.J.D. Lindan, M.J. Probert, C.J. Pickard, P.J. Hasnip, S.J. Clark, M.C. Payne, First-principles simulation: ideas, illustrations and the CASTEPcode, *Journal of Physics: Condensed Matter* 14 (2002) 2717. <https://doi.org/10.1088/0953-8984/14/11/301>.
- [41] B.G. Pfrommer, M. Côté, S.G. Louie, M.L. Cohen, Relaxation of Crystals with the Quasi-Newton Method, *J Comput Phys* 131 (1997) 233–240. <https://doi.org/10.1006/JCPH.1996.5612>.
- [42] M.C. Payne, M.P. Teter, D.C. Allan, T.A. Arias, J.D. Joannopoulos, Iterative minimization techniques for *ab initio* total-energy calculations: molecular dynamics and conjugate gradients, *Rev Mod Phys* 64 (1992) 1045. <https://doi.org/10.1103/RevModPhys.64.1045>.
- [43] S.M. Hosseini, T. Movlaroooy, A. Kompany, First-principle calculations of the cohesive energy and the electronic properties of  $\text{PbTiO}_3$ , *Physica B Condens Matter* 391 (2007) 316–321. <https://doi.org/10.1016/J.PHYSB.2006.10.013>.
- [44] B. Ghebouli, M.A. Ghebouli, M. Fatmi, Structural, elastic, electronic, optical and thermal properties of cubic perovskite  $\text{CsCdF}_3$  under pressure effect, *The European Physical Journal Applied Physics* 53 (2011) 30101. <https://doi.org/10.1051/EPJAP/2010100318>.
- [45] M. Segall, R. Shah, C. Pickard, M. Payne, Population analysis of plane-wave electronic structure calculations of bulk materials, *Phys Rev B* 54 (1996) 16317. <https://doi.org/10.1103/PhysRevB.54.16317>.
- [46] Z. Ali, I. Ahmad, B. Khan, I. Khan, Robust Half-Metallicity and Magnetic Properties of Cubic Perovskite  $\text{CaFeO}_3$ , *Chinese Physics Letters* 30 (2013) 047504. <https://doi.org/10.1088/0256-307X/30/4/047504>.



- [47] Z. Ali, I. Ahmad, B. Amin, M. Maqbool, G. Murtaza, I. Khan, M.J. Akhtar, F. Ghaffor, Theoretical studies of structural and magnetic properties of cubic perovskites  $\text{PrCoO}_3$  and  $\text{NdCoO}_3$ , *Physica B Condens Matter* 406 (2011) 3800–3804. <https://doi.org/10.1016/J.PHYSB.2011.06.065>.
- [48] S.A. Khandy, D.C. Gupta, DFT analogue of prospecting the spin-polarised properties of layered perovskites  $\text{Ba}_2\text{ErNbO}_6$  and  $\text{Ba}_2\text{TmNbO}_6$  influenced by electronic structure, *Sci Rep* 12 (2022) 1–14. <https://doi.org/10.1038/S41598-022-22070-X>;
- [49] P. Dufek, P. Blaha, K. Schwarz, Applications of Engel and Vosko's generalized gradient approximation in solids, *Phys Rev B* 50 (1994) 7279. <https://doi.org/10.1103/PhysRevB.50.7279>.
- [50] D. Koller, F. Tran, P. Blaha, Improving the modified Becke-Johnson exchange potential, *Phys Rev B Condens Matter Mater Phys* 85 (2012) 155109. <https://doi.org/10.1103/PHYSREVB.85.155109/FIGURES/6/THUMBNAI>.
- [51] P. Nayak, D.C. Gupta, Exploring the multifaceted properties: electronic, magnetic, Curie temperature, elastic, thermal, and thermoelectric characteristics of gadolinium-filled  $\text{PtSb}_3$  skutterudite, *RSC Adv* 14 (2024) 17364–17379. <https://doi.org/10.1039/D4RA01303D>.
- [52] J.M. Leger, C. Loriers-Susse, B. Vodar, Pressure Effect on the Curie Temperatures of Transition Metals and Alloys, *Phys Rev B* 6 (1972) 4250. <https://doi.org/10.1103/PhysRevB.6.4250>.
- [53] B. Aladerah, M. Gharaibeh, A. Obeidat, K. Aledealat, A comparative study of structural, electronic, magnetic, and pressure-dependent properties of Full-Heusler  $\text{Fe}_2\text{XSi}$  (X=Mn and Co): first-principles calculation and Monte Carlo Simulation, *Phys Scr* 98 (2023) 085954. <https://doi.org/10.1088/1402-4896/ACE8CE>.
- [54] W. Chen, J. George, J.B. Varley, G.M. Rignanese, G. Hautier, High-throughput computational discovery of  $\text{In}_2\text{Mn}_2\text{O}_7$  as a high Curie temperature ferromagnetic semiconductor for spintronics, *NPJ Comput Mater* 5 (2019) 1–7. <https://doi.org/10.1038/S41524-019-0208-X>;
- [55] N. Moulay, M. Ameri, Y. Azaz, A. Zenati, Y. Al-Douri, I. Ameri, Predictive study of structural, electronic, magnetic and thermodynamic properties of  $\text{XFeO}_3$  (X = Ag, Zr and Ru) multiferroic materials in cubic perovskite structure: First-principles calculations, *Materials Science- Poland* 33 (2015) 402–413. <https://doi.org/10.1515/MSP-2015-0047>.
- [56] Z. Ali, I. Ahmad, B. Khan, I. Khan, Robust Half-Metallicity and Magnetic Properties of Cubic Perovskite  $\text{CaFeO}_3$ , *Chinese Physics Letters* 30 (2013) 047504. <https://doi.org/10.1088/0256-307X/30/4/047504>.
- [57] A. Jabar, S. Benyoussef, L. Bahmad, Study of Physical Characteristics of the New Half-Heusler Alloy  $\text{BaHgSn}$  by DFT Analysis, (2024). <https://arxiv.org/pdf/2403.08483> (accessed June 15, 2025).
- [58] R.A. De Groot, F.M. Mueller, P.G.V. Engen, K.H.J. Buschow, New Class of Materials: Half-Metallic Ferromagnets, *Phys Rev Lett* 50 (1983) 2024. <https://doi.org/10.1103/PhysRevLett.50.2024>.
- [59] R.K. Pingak, S. Bouhmaidi, L. Setti, B. Pasangka, B. Bernandus, H.I. Sutaji, F. Nitti, M.Z. Ndi, Structural, Electronic, Elastic, and Optical Properties of Cubic  $\text{BaLiX}_3$  (X = F, Cl, Br, or I) Perovskites: An Ab-initio DFT Study, *Indonesian Journal of Chemistry* 23 (2023) 843–862. <https://doi.org/10.22146/IJC.83261>.
- [60] Z.J. Wu, E.J. Zhao, H.P. Xiang, X.F. Hao, X.J. Liu, J. Meng, Crystal structures and elastic properties of superhard  $\text{Ir N}_2$  and  $\text{Ir N}_3$  from first principles, *Phys Rev B Condens Matter*



- Mater Phys 76 (2007) 054115.  
<https://doi.org/10.1103/PHYSREVB.76.054115/FIGURES/12/THUMBNAI>.
- [61] S. Goumri-Said, M.B. Kanoun, Theoretical investigations of structural, elastic, electronic and thermal properties of Damiaoite  $\text{PtIn}_2$ , *Comput Mater Sci* 43 (2008) 243–250. <https://doi.org/10.1016/J.COMMATSCI.2007.10.009>.
- [62] J. Gao, Q.J. Liu, B. Tang, Elastic stability criteria of seven crystal systems and their application under pressure: Taking carbon as an example, *J Appl Phys* 133 (2023). <https://doi.org/10.1063/5.0139232>.
- [63] M.J. Mehl, Pressure dependence of the elastic moduli in aluminum-rich Al-Li compounds, *Phys Rev B* 47 (1993) 2493. <https://doi.org/10.1103/PhysRevB.47.2493>.
- [64] Z. Sun, S. Li, R. Ahuja, J.M. Schneider, Calculated elastic properties of  $\text{M}_2\text{AlC}$  (M=Ti, V, Cr, Nb and Ta), *Solid State Commun* 129 (2004) 589–592. <https://doi.org/10.1016/J.SSC.2003.12.008>.
- [65] C. Jasiukiewicz, V. Karpus, Debye temperature of cubic crystals, *Solid State Commun* 128 (2003) 167–169. <https://doi.org/10.1016/J.SSC.2003.08.008>.
- [66] P. Wachter, M. Filzmoser, J. Rebizant, Electronic and elastic properties of the light actinide tellurides, *Physica B Condens Matter* 293 (2001) 199–223. [https://doi.org/10.1016/S0921-4526\(00\)00575-5](https://doi.org/10.1016/S0921-4526(00)00575-5).
- [67] M.J. Mehl, J.E. Osburn, D.A. Papaconstantopoulos, B.M. Klein, Structural properties of ordered high-melting-temperature intermetallic alloys from first-principles total-energy calculations, *Phys Rev B* 41 (1990) 10311. <https://doi.org/10.1103/PhysRevB.41.10311>.
- [68] R. Majumder, M.M. Hossain, D. Shen, First-principles study of structural, electronic, elastic, thermodynamic and optical properties of LuPdBi half-Heusler compound, <https://doi.org/10.1142/S0217984919503780>.
- [69] M.A. Ali, R. Ullah, S.A. Dar, G. Murtaza, A. Khan, A. Mahmood, Modeling of structural, elastic, mechanical, acoustical, electronic and thermodynamic properties of  $\text{XPdF}_3$  (X = Rb, Tl) perovskites through density functional theory, *Phys Scr* 95 (2020). <https://doi.org/10.1088/1402-4896/AB8EEE>.
- [70] L. Vitos, P.A. Korzhavyi, B. Johansson, Stainless steel optimization from quantum mechanical calculations, *Nat Mater* 2 (2003) 25–28. <https://doi.org/10.1038/NMAT790>.
- [71] X.Q. Chen, H. Niu, D. Li, Y. Li, Modeling hardness of polycrystalline materials and bulk metallic glasses, *Intermetallics (Barking)* 19 (2011) 1275–1281. <https://doi.org/10.1016/J.INTERMET.2011.03.026>.
- [72] G. Dresselhaus, The fermi surface and optical properties of copper, *Solid State Commun* 7 (1969) 419–423. [https://doi.org/10.1016/0038-1098\(69\)90887-4](https://doi.org/10.1016/0038-1098(69)90887-4).
- [73] R. Majumder, M.M. Hossain, D. Shen, First-principles study of structural, electronic, elastic, thermodynamic and optical properties of LuPdBi half-Heusler compound, <https://doi.org/10.1142/S0217984919503780>.
- [74] M.K. Butt, M. Yaseen, J. Iqbal, A.S. Altowyan, A. Murtaza, M. Iqbal, A. Laref, Structural, electronic, half –metallic ferromagnetic and optical properties of cubic  $\text{MAIO}_3$  (M=Ce, Pr) perovskites: A DFT study, *Journal of Physics and Chemistry of Solids* 154 (2021) 110084. <https://doi.org/10.1016/J.JPCS.2021.110084>.
- [75] Oxford Master Series in Condensed Matter Physics Atomic , Optical , and Laser Physics Particle Physics , Astrophysics , and Cosmology, (n.d.). <https://global.oup.com/academic/product/optical-properties-of-solids-9780199573363> (accessed June 15, 2025).



- [76] G. Murtaza, I. Ahmad, First principle study of the structural and optoelectronic properties of cubic perovskites  $\text{CsPbM}_3$  ( $\text{M}=\text{Cl}, \text{Br}, \text{I}$ ), *Physica B Condens Matter* 406 (2011) 3222–3229. <https://doi.org/10.1016/J.PHYSB.2011.05.028>.
- [77] Electronic structure, chemical bonding, and optical properties of ferroelectric and antiferroelectric | *Phys. Rev. B*, (n.d.). <https://journals.aps.org/prb/abstract/10.1103/PhysRevB.59.1776> (accessed June 15, 2025).
- [78] B.D. Pennington, Infrared Spectroscopy in Analysis of Polymer Structure–Property Relationships, *Encyclopedia of Analytical Chemistry* (2000). <https://doi.org/10.1002/9780470027318.A2014>.
- [79] A. Hossain, M.S.I. Sarker, M.K.R. Khan, M.M. Rahman, Spin effect on electronic, magnetic and optical properties of spinel  $\text{CoFe}_2\text{O}_4$ : A DFT study, *Materials Science and Engineering: B* 253 (2020) 114496. <https://doi.org/10.1016/J.MSEB.2020.114496>.
- [80] S. Subburaj, B. Arumugam, S.M. Chen, T.W. Chen, A. Seetharam, S.K. Ramaraj, Polyol synthesis of Ag Nanowires as an electrochemical sensor for the quantification of Carcinogenic Hydrazine, *Int J Electrochem Sci* 16 (2021) 210773. <https://doi.org/10.20964/2021.07.74>.

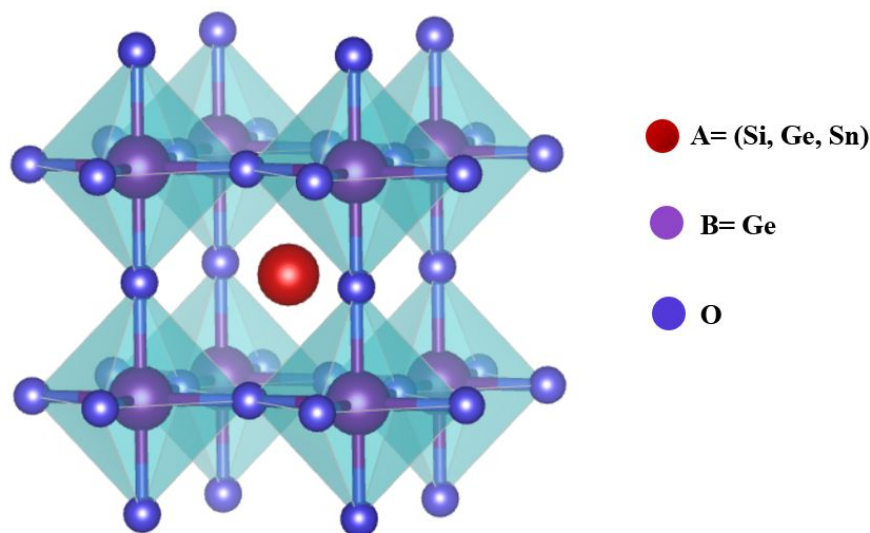


Figure-1: The cubic crystallographic unit cell of  $\text{ACrO}_3$  ( $\text{A} = \text{Si}, \text{Ge}, \text{Sn}$ ).



Table 1: Calculated lattice constant  $a(A)$ , equilibrium volume  $V_0$ , normalized lattice parameter, and volume.

Compounds	Parameter	0-GPa	10-GPa	20-GPa	30-GPa
SiCrO <sub>3</sub>	Energy $E_{FM}$ (eV)	-3885.06	-3884.90	-3884.77	-3884.68
	Energy $E_{NM}$ (eV)	-3884.74	-3884.74	-3884.64	-3884.47
	Spin polarized Lattice constant $a(A)$	3.79	3.70	3.65	3.60
	Non-spin polarized Lattice constant $a(A)$	3.75	3.69	3.65	3.61
	Volume (FM) $V_0$	54.57	50.52	48.79	46.93
	Volume (NM) $V_0$	53.07	50.49	48.73	47.11
	Normalized lattice parameter $a/a_0$	1	0.97	0.96	0.94
	Normalized volume $V/V_0$	1	0.92	0.89	0.85
GeCrO <sub>3</sub>	Energy $E_{FM}$ (eV)	-6253.95	-6253.88	-6253.76	-6253.70
	Energy $E_{NM}$ (eV)	-6253.75	-6253.71	-6253.62	-6253.57
	Spin polarized Lattice constant $a(A)$	3.81	3.74	3.69	3.66
	Non-spin polarized Lattice constant $a(A)$	3.78	3.72	3.67	3.63
	Volume (FM) $V_0$	55.63	52.72	50.58	49.09
	Volume (NM) $V_0$	54.40	51.58	49.61	47.94
	Normalized lattice parameter $a/a_0$	1	0.98	0.968	0.960
	Normalized volume $V/V_0$	1	0.94	0.90	0.88
SnCrO <sub>3</sub>	Energy $E_{FM}$ (eV)	-5765.26	-5765.08	-5764.89	-5764.56
	Energy $E_{NM}$ (eV)	-5764.98	-5764.89	-5764.74	-6764.44
	Spin polarized Lattice constant $a(A)$	3.87	3.81	3.72	3.68
	Non-spin polarized Lattice constant $a(A)$	3.84	3.77	3.72	3.68
	Volume (FM) $V_0$	58.29	55.60	51.78	49.85
	Volume (NM) $V_0$	56.91	53.95	51.77	49.85
	Normalized lattice parameter $a/a_0$	1	0.98	0.96	0.950
	Normalized volume $V/V_0$	1	0.953	0.88	0.855





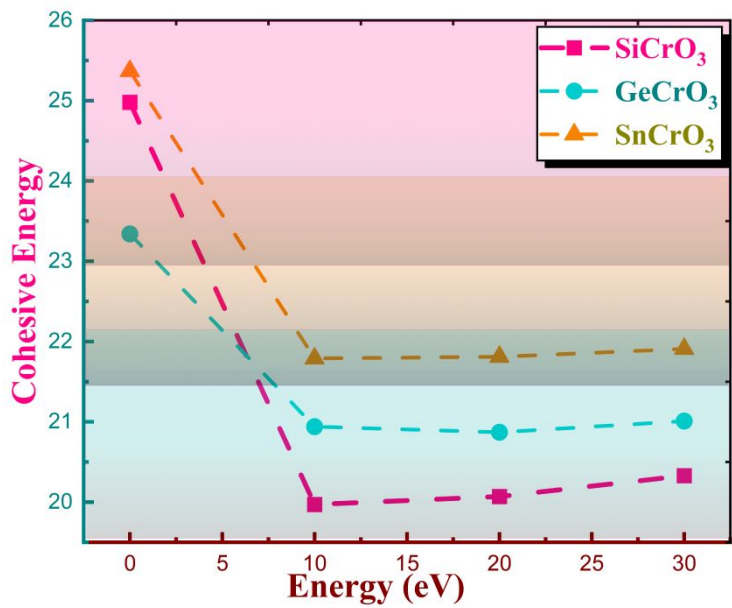


Table-2: The cohesive energy of cubic ACrO<sub>3</sub> (A = Si,Ge,Sn) compounds at different pressure.

Cohesive Energy	Structure	0-GPa	10-GPa	20-GPa	30-GPa
	SiCrO <sub>3</sub>	24.98	19.97	20.07	20.33
	GeCrO <sub>3</sub>	23.34	20.94	20.87	21.01
	SnCrO <sub>3</sub>	25.37	21.79	21.81	21.91

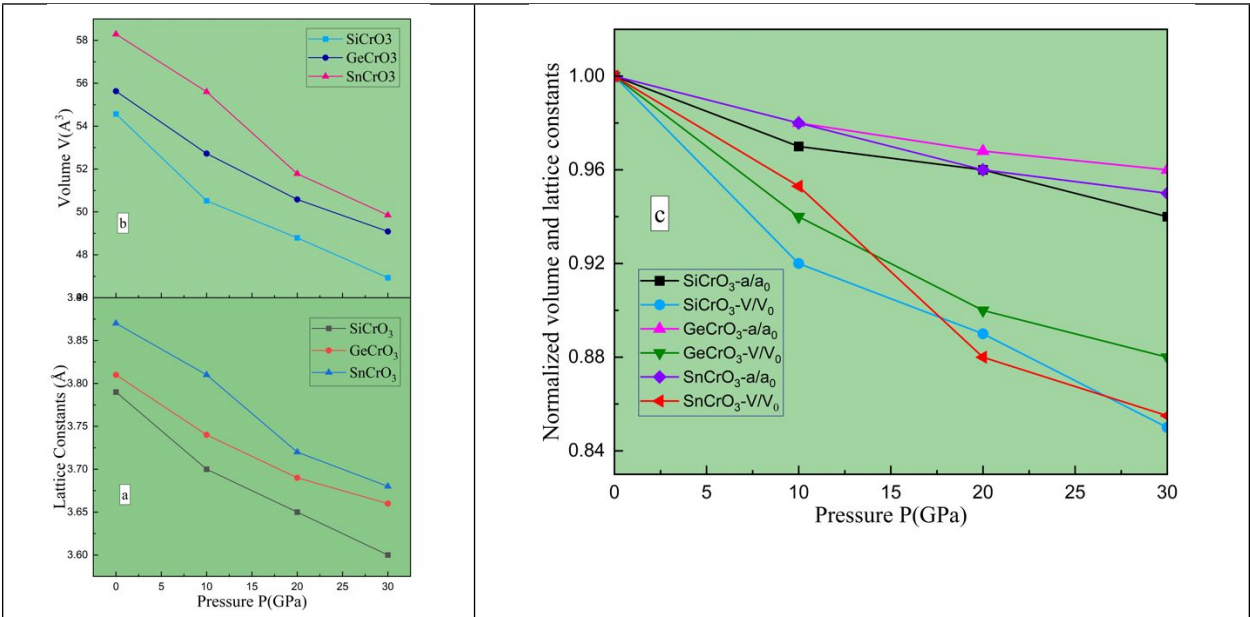
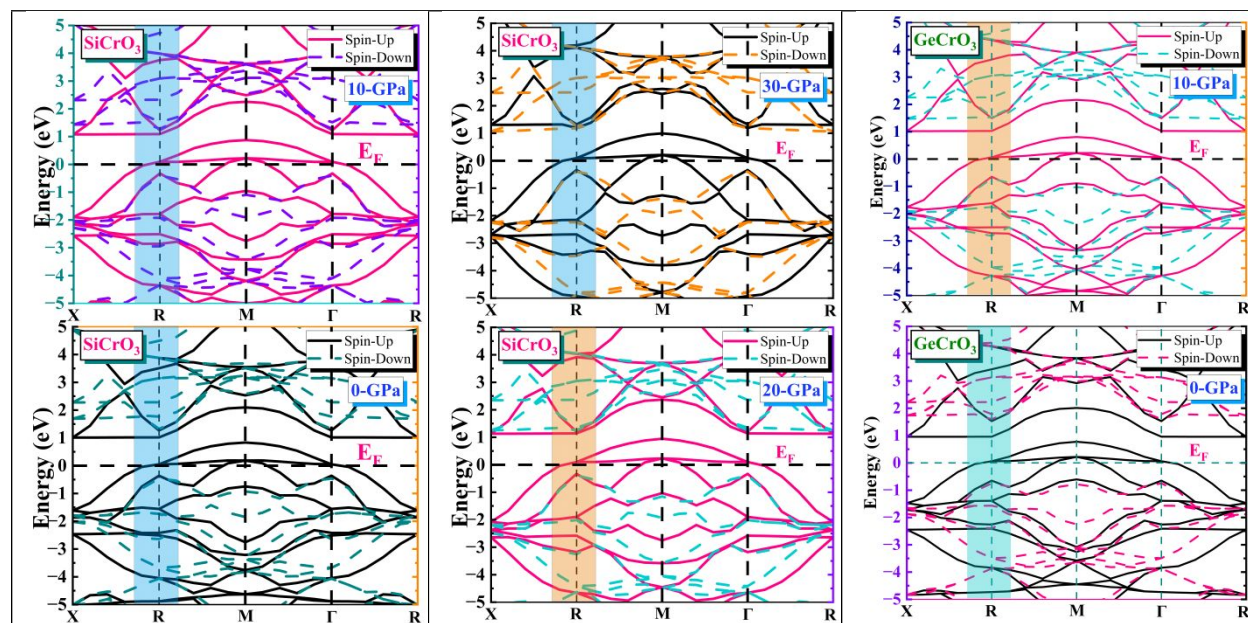




Figure 2: (a) Variations of lattice parameter and (b) cell volume and (c) normalized lattice parameter and volume of  $ACrO_3$  ( $A = Si, Ge, Sn$ ) as a function of pressure.

Table 3: Mulliken charges, bond lengths, and bond populations analysis of  $ACrO_3$  ( $A = Si, Ge, Sn$ ) from the GGA method.

	Species	s	P	d	Total	Charge(electron)	Bond	Popolation	Bond lengths(Å)	Tolerance Factor(t)
SiCrO <sub>3</sub>	Si	2.04	1.06	0	3.10	0.90	O-Si	0.03	2.60	0.97
	Cr	2.28	6.39	4.44	13.10	0.89	O-Cr	0.85	1.88	
	O	1.85	4.75	0	6.60	-0.60				
GeCrO <sub>3</sub>	Ge	1.71	1.07	10	12.78	1.22	O-Ge	-0.16	2.69	1.009
	Cr	2.44	6.58	4.31	13.33	0.67	O-Cr	1.05	1.90	
	O	1.85	4.78	0	6.63	-0.63				
SnCrO <sub>3</sub>	Sn	1.98	0.95	10.0	12.94	1.06	O-Sn	0.06	2.74	0.999
	Cr	2.31	6.45	4.30	13.06	0.94	O-Cr	0.82	1.93	
	O	1.85	4.82	0	6.67	-0.67				



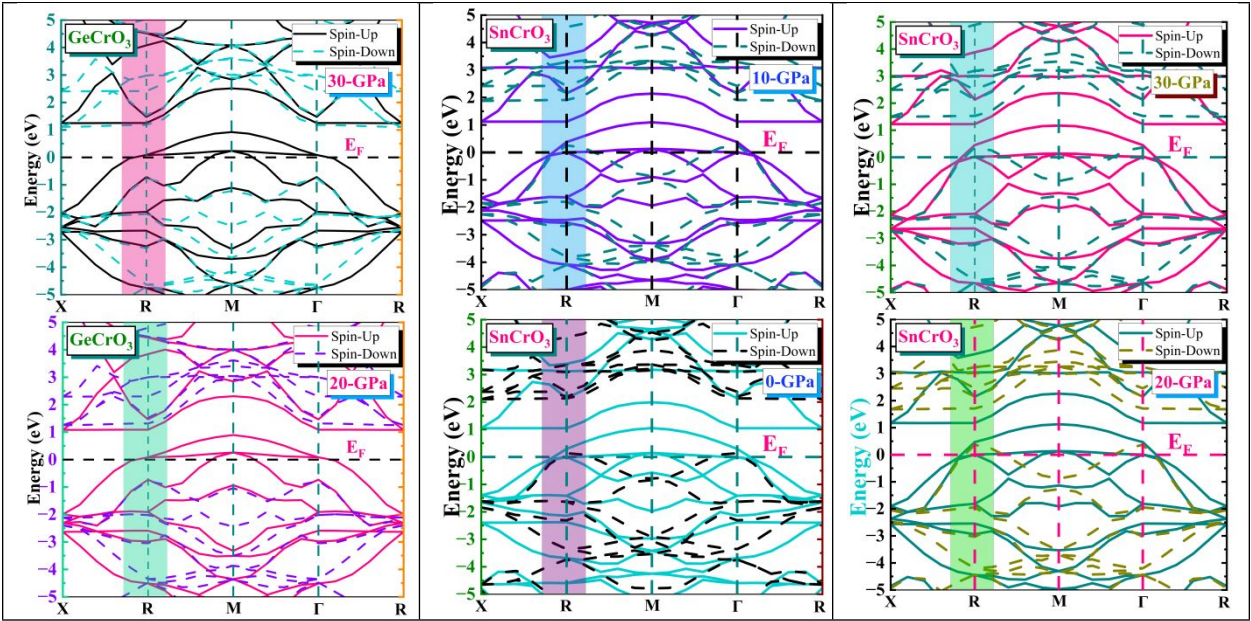


Figure 3: Predicted Spin-polarized Band structure of  $ACrO_3$  ( $A = Si, Ge, Sn$ ) under hydrostatic pressure 0-30 GPa using GGA+U functional.



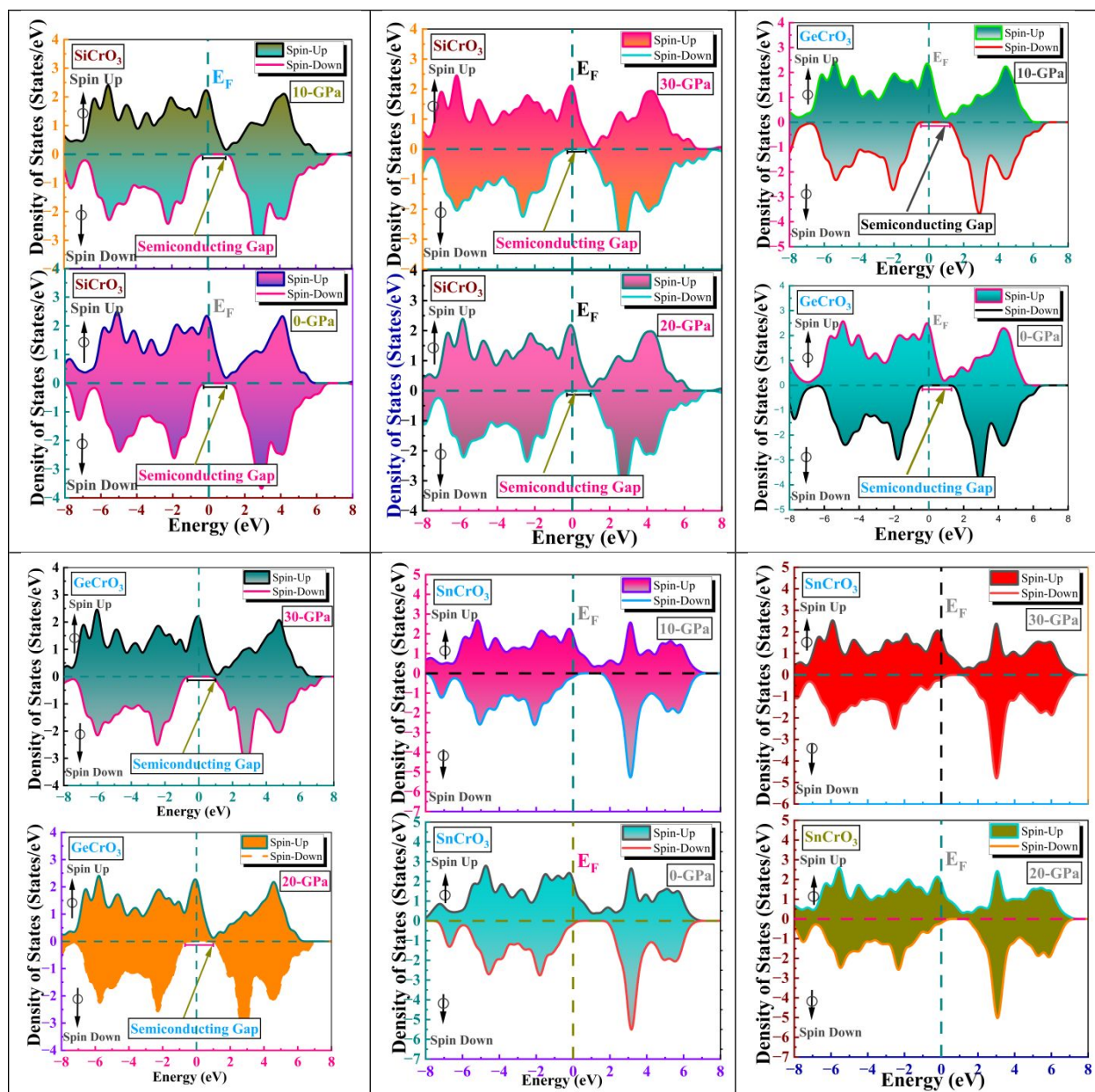


Figure 5: Density of states (DOS) for GGA in the cubic structure of  $ACrO_3$  ( $A = \text{Si, Ge, Sn}$ ).





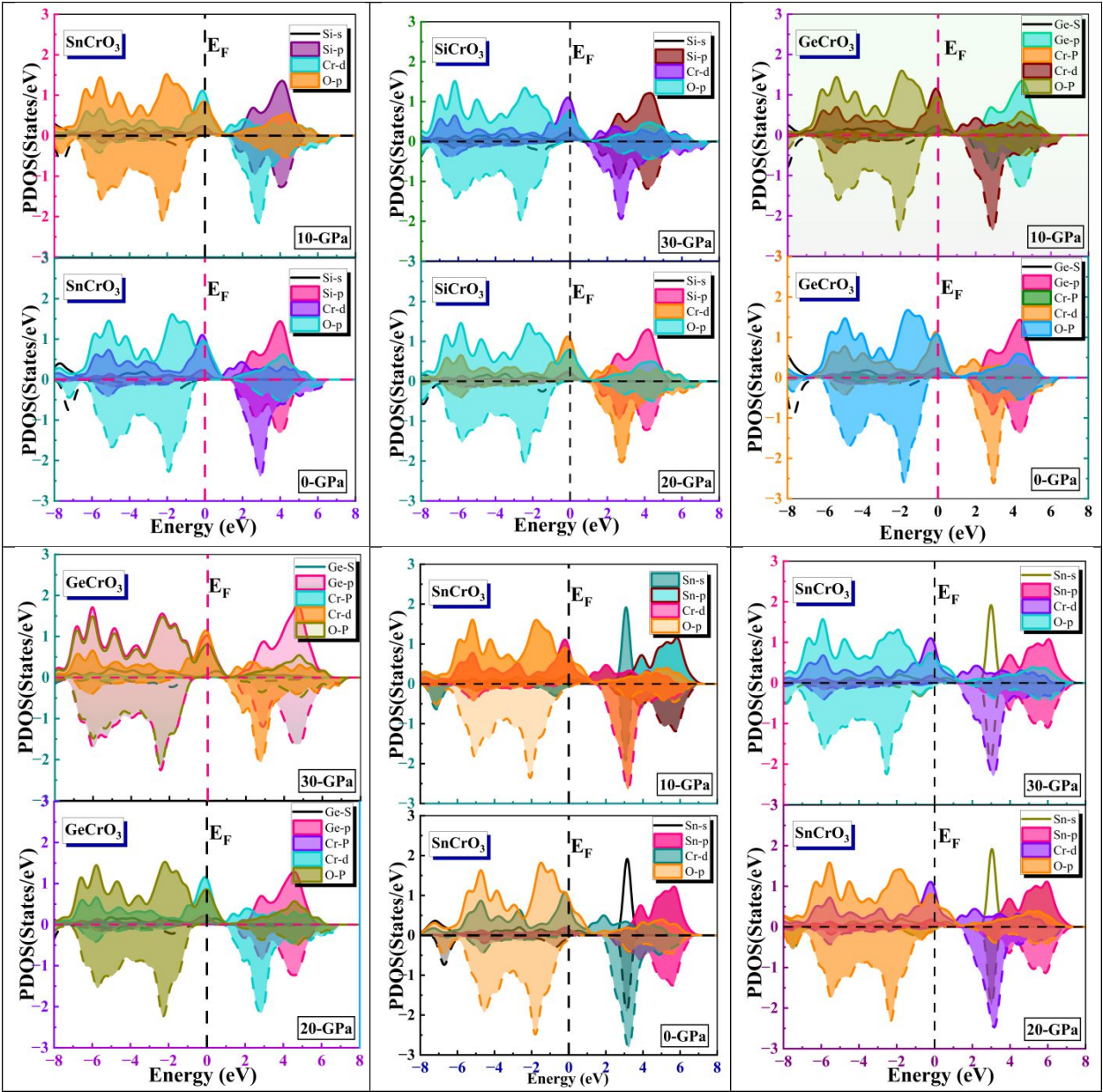


Figure 6: Spin polarized partial density of states (PDOS) of cubic  $ACrO_3$  ( $A = Si, Ge, Sn$ ) at various pressure.



Table-4: Spin magnetic moment and Curie temperature at various pressure.

	Magnetic moment	0-GPa	10-GPa	20-GPa	30-GPa
SiCrO <sub>3</sub>	Moment- $\mu_{\text{O}}$	0.03	0.09	0.12	0.12
	Moment- $\mu_{\text{Si}}$	0.06	0.07	0.07	0.07
	Moment- $\mu_{\text{Cr}}$	1.90	1.85	1.83	1.81
	Total $\mu$	1.99	2.01	2.02	2.01
	Curie Temperature T <sub>C</sub> (K)	1236.71	616.35	502.41	386.47
GeCrO <sub>3</sub>	Moment- $\mu_{\text{O}}$	0.03	0.09	0.12	0.12
	Moment- $\mu_{\text{Ge}}$	0.06	0.07	0.07	0.07
	Moment- $\mu_{\text{Cr}}$	1.90	1.85	1.81	1.81
	Total $\mu$	1.99	2.01	2.0	2.0
	Curie Temperature T <sub>C</sub> (K)	772.94	657	541.06	502.41
SnCrO <sub>3</sub>	Moment- $\mu_{\text{O}}$	-0.03	0.03	0.03	0.03
	Moment- $\mu_{\text{Sn}}$	0	0	0	0
	Moment- $\mu_{\text{Cr}}$	2.02	1.98	0.47	0.47
	Total $\mu$	1.99	2.01	0.50	0.50
	Curie Temperature T <sub>C</sub> (K)	1082.12	734.29	579.70	463.76

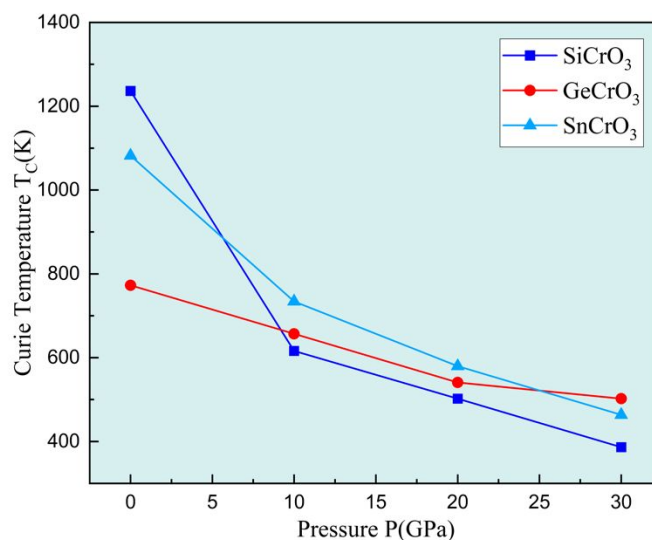


Figure 7: The relation between Curie temperature and pressure in (GPa).



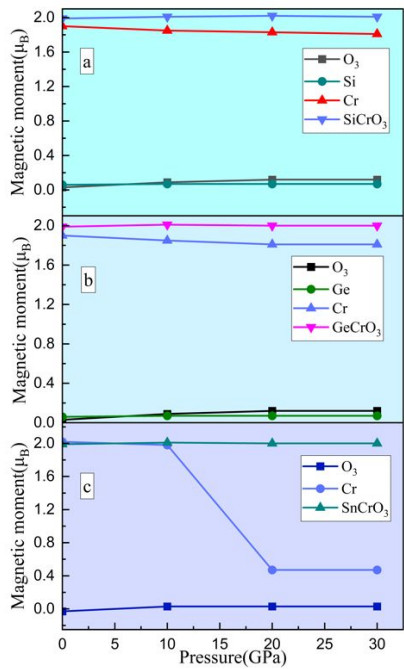


Figure-8: Effect of pressure on magnetic moments at  $O_3$ , Cr, Si, Ge, and Sn atomic sites for  $ACrO_3$  ( $A = Si, Ge, Sn$ ) multiferroic materials in GGA calculations.

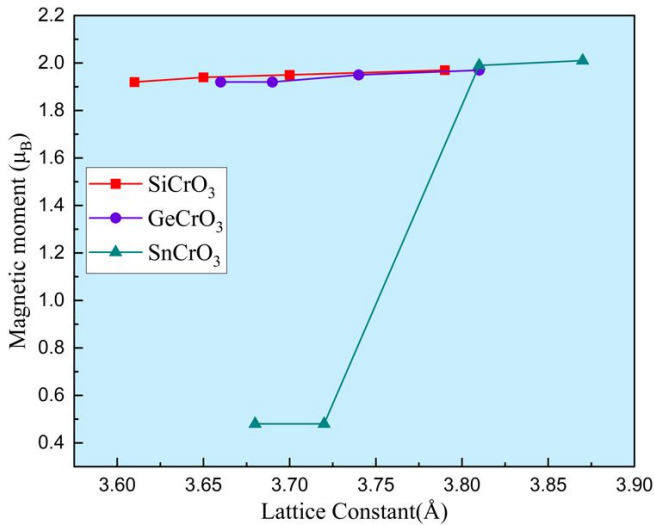


Figure 9: (a) Spin moment versus lattice constants of  $ACrO_3$  ( $A = Si, Ge, Sn$ ).

--	--



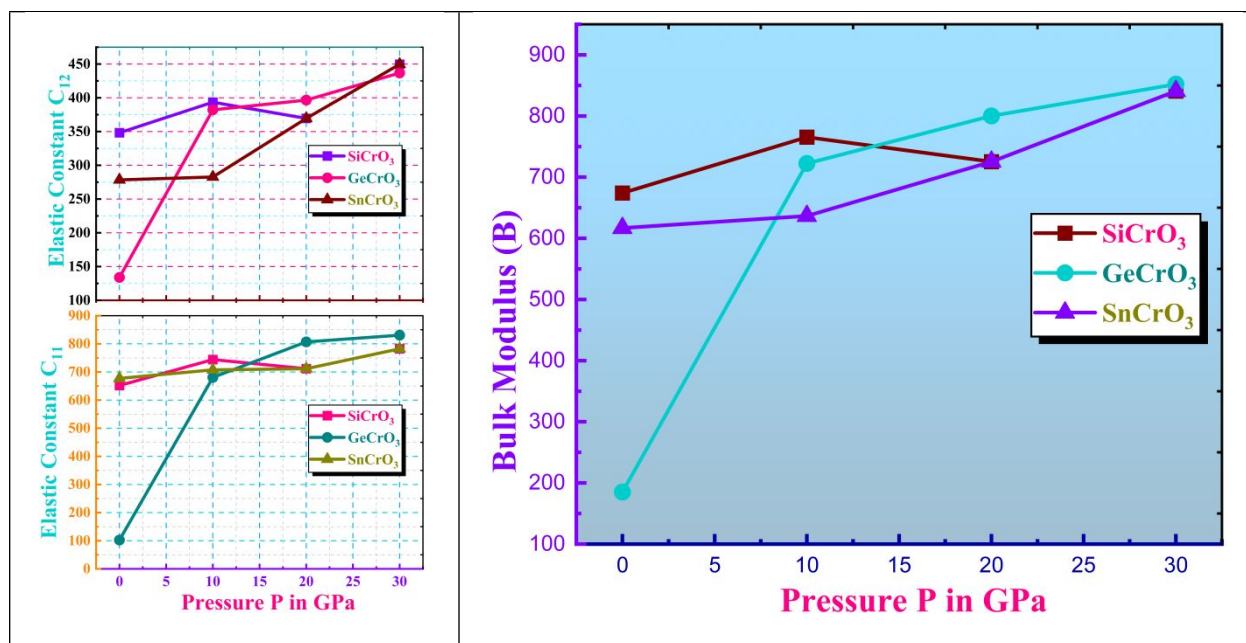


Figure 10: Changes in elastic constants parameter and (Right) Bulk modulus(B) of  $\text{ACrO}_3$  (A = Si,Ge,Sn) subjected to different hydrostatic pressures.

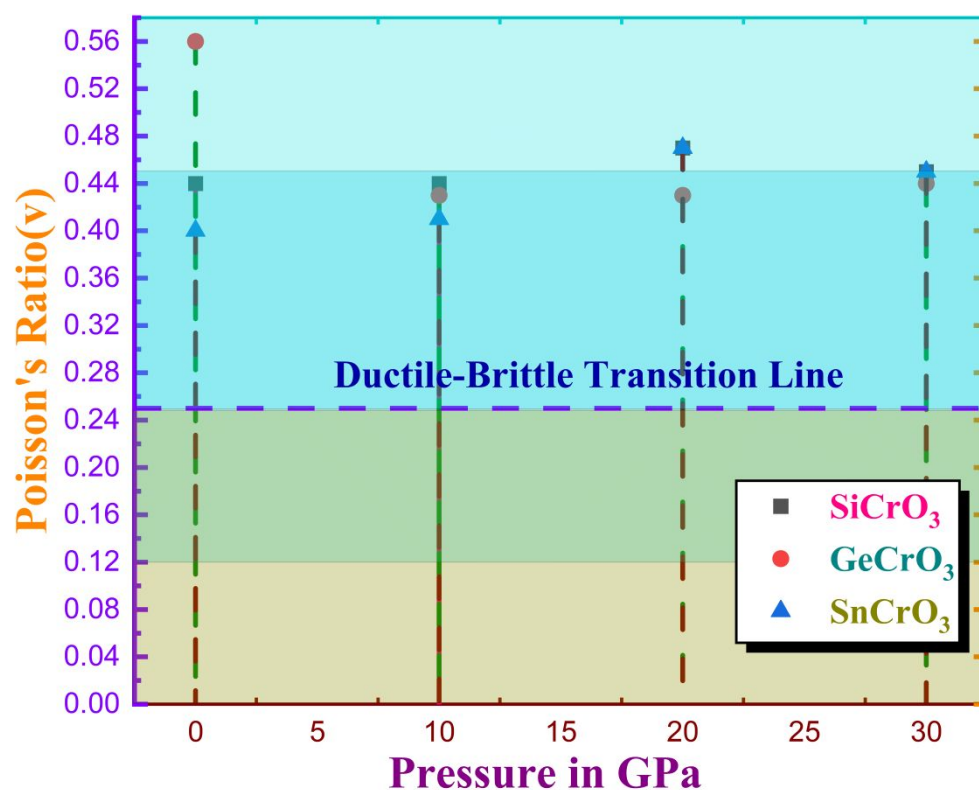


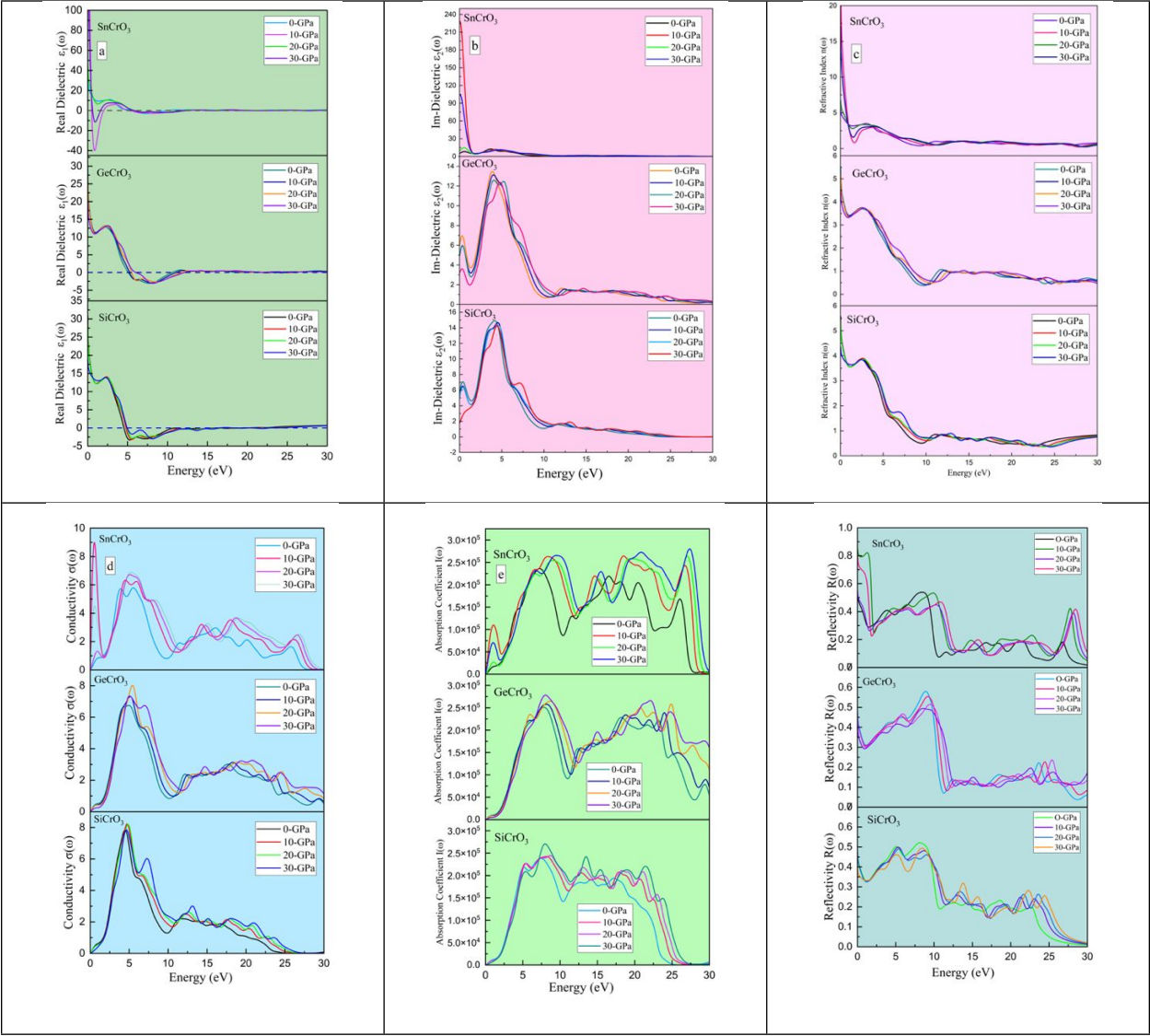
Figure 11: Ductile-brittle behavior of  $\text{ACrO}_3$  ( $A = \text{Si, Ge, Sn}$ ) at different pressures.

Table 5: Bulk modulus  $B$  (GPa), shear modulus  $G$  (GPa), Young's modulus  $E$  (GPa), hardness (GPa), plasticity measurement ( $B/C_{44}$ ), Pugh's ratio( $B/G$ ), ( $C_{11}-C_{44}$ ) Cauchy pressure (GPa), Poisson's ratio ( $\nu$ ), Kleinman parameter ( $\zeta$ ) and Zener anisotropy factor ( $A$ ) of  $\text{ACrO}_3$  ( $A = \text{Si, Ge, Sn}$ ) compound.

Compounds	Elastic parameters	0 Pa	10 Gpa	20 Gpa	30 Gpa
SiCrO <sub>3</sub>	$C_{11}$	651.77	744.04	711.45	782.30
	$C_{12}$	348.24	393.47	369.52	449.62
	$C_{44}$	60.88	68.21	2.47	56.31
	Bulk modulus (B)	674.12	765.49	725.24	840.77
	Shear modulus(voigt) $G_V$	72.88	83.75	68.88	77.79
	Shear modulus(Reuss) $G_R$	80.05	90.26	4.07	76.56
	Shear modulus((Hill) $G$	76.46	87.01	36.47	77.18
	Young modulus(Hill) $E$	221.05	251.50	107.63	224.67
	Cauchy pressure ( $C_{12}-C_{44}$ )	287.36	325.26	367.05	393.31
	Kleinman parameter ( $\zeta$ )	0.65	0.64	0.64	0.68
	Pugh's ratio ( $B/G$ )	8.81	8.79	19.88	10.89
	Poisson ratio ( $\nu$ )	0.44	0.44	0.47	0.45
	Plasticity measurement ( $B/C_{44}$ )	11.07	11.22	293.62	14.93
	Anisotropy Factor ( $A$ )	0.40	0.38	0.01	0.33
GeCrO <sub>3</sub>	Dynamical Stability	Stable	Stable	Unstable	Stable
	$C_{11}$	102.49	680.65	806.98	830.71
	$C_{12}$	133.87	382.18	396.60	436.79
	$C_{44}$	75.06	89.95	85.52	86.39
	Bulk modulus (B)	185.11	722.5	800.09	852.14
	Shear modulus(voigt) $G_V$	8.73	77.68	99.18	96.06
	Shear modulus(Reuss) $G_R$	-57.18	106.94	111.54	111.14
	Shear modulus((Hill) $G$	-24.20	92.31	105.36	103.73
	Young modulus(Hill) $E$	-75.91	265.62	302.79	299.06
	Cauchy pressure ( $C_{12}-C_{44}$ )	58.81	292.23	311.08	350.4
	Kleinman parameter ( $\zeta$ )	1.19	0.67	0.61	0.64
	Pugh's ratio ( $B/G$ )	-7.64	7.82	7.59	8.21
	Poisson ratio ( $\nu$ )	0.56	0.43	0.43	0.44
	Plasticity measurement ( $B/C_{44}$ )	2.46	8.03	9.35	9.86
	Anisotropy Factor ( $A$ )	-4.78	0.6	0.41	0.43
	Dynamical Stability	Stable	Stable	Stable	Stable
	$C_{11}$	677.05	707.66	711.45	782.30
	$C_{12}$	278.44	282.71	369.52	449.62
	$C_{44}$	126.53	92.78	2.47	56.31
	Bulk modulus (B)	616.96	636.54	725.24	840.77
	Shear modulus(voigt) $G_V$	105.02	103.54	68.88	77.79
	Shear modulus(Reuss) $G_R$	148.17	119.76	4.07	76.56
	Shear modulus((Hill) $G$	126.59	111.65	36.47	77.18
	Young modulus(Hill) $E$	355.48	316.46	107.63	224.67



SnCrO <sub>3</sub>	Cauchy pressure ( $C_{12}-C_{44}$ )	151.91	189.93	367.05	393.31
	Kleinman parameter ( $\zeta$ )	0.54	0.53	0.64	0.68
	Pugh's ratio ( $B/G$ )	4.87	5.70	19.88	10.89
	Poisson ratio ( $\nu$ )	0.40	0.41	0.475	0.455
	Plasticity measurement ( $B/C_{44}$ )	4.87	6.86	293.62	14.93
	Anisotropy Factor ( $A$ )	0.63	0.43	0.01	0.33
	Dynamical Stability	Stable	Stable	Unstable	Stable



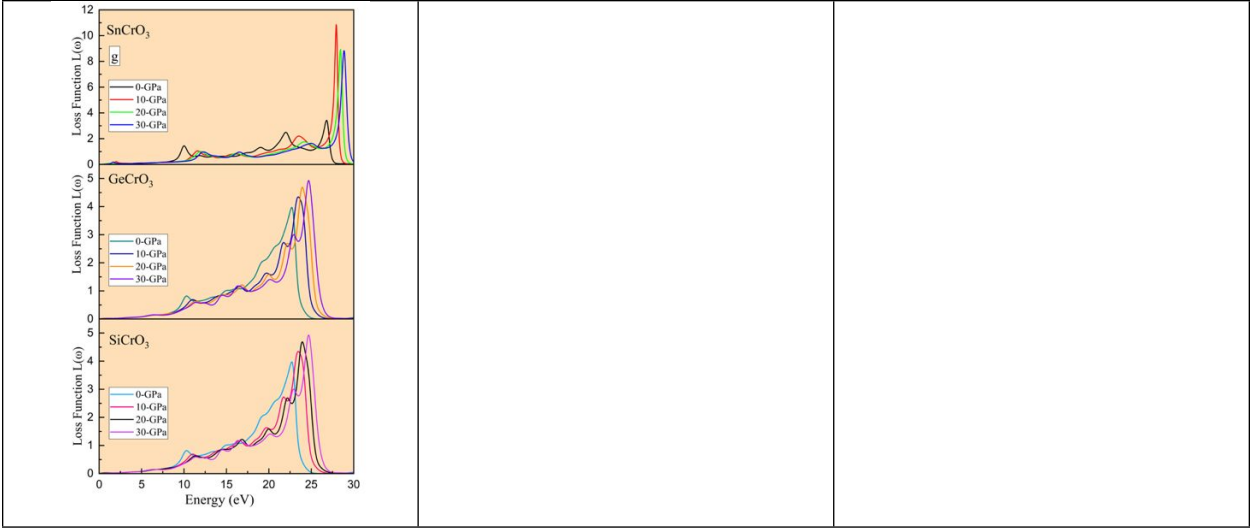


Figure 12: Energy-dependent optical parameters of  $ACrO_3$  ( $A = \text{Si, Ge, Sn}$ ) at various pressures.



## Data Availability Statement

The data supporting this article have been included as part of the Supplementary Information.

